journal of the international meteor organization

WGN

48:1
february 2020

ISSN 1016-3115

WGN Vol. 48, No. 1, February 2020, pp. 1 – 24

Administrative

Radio meteors

Preliminary results

Meteor Beliefs

Front cover photo

Perseid fireball captured on 2016 August 11 from Kolob, Utah, USA. Notice the several flares along its path. Photo courtesy: David Whalen.

Writing for WGN

This Journal welcomes papers submitted for publication. All papers are reviewed for scientific content, and edited for English and style. Instructions for authors can be found in WGN **45:1**, 1–5, and at `http://www.imo.net/docs/writingforwgn.pdf` .

Copyright

Legal address

International Meteor Organization, Jozef Mattheessensstraat 60, 2540 Hove, Belgium.

Janus

Cis Verbeeck[1]

More and more data...

The worldwide coverage of meteor and fireball observations has been extending and extending for many years, and this was not different in 2019. On the higher end of the spectrum, the following events were observed in 2019:

- On February 1, a bright fireball was observed over Western Cuba, followed by a vapor condensation trail that persisted for several minutes. Tens of seconds later, a huge sonic boom was heard, and meteorites of up to 7 cm in diameter were recovered near Viñales, northwest of Pinar del Rio, Western Cuba.
- A bright fireball was captured on May 19 by multiple cameras from Northern Territory in Australia, by infrasound stations, and by stations of the International Monitoring System of the Comprehensive Nuclear-Test-Ban Treaty Organisation (CTBTO). Its estimated energy of 60 t TNT and diameter of about 1.2 m place it in the asteroid range.
- On May 21, another bright fireball was observed over Southern Australia and detected by cameras and 6 infrasound stations, which yielded an estimated energy of 1.4 kt TNT and an estimated asteroid diameter of about 4 m.
- An asteroid was detected on June 22 with all kinds of sensors — infrasound arrays, a lightning mapper, and even a ground-based telescope — before it entered the Earth's atmosphere over the Caribbean. With an estimated energy of 2.5 kt TNT, its diameter would be about 4.5 m.
- A bright fireball was observed over the western-central Mediterranean Sea on August 16 with an estimated energy of 0.1 kt TNT and an estimated asteroid diameter of about 1.4 m.
- A bright fireball was observed on September 12 over Northern Germany, with 584 fireball reports submitted to IMO. It had an estimated energy of 0.48 kt TNT, corresponding to an asteroid of about 2 m diameter.

IMO has been gathering worldwide fireball reports and showing the results at `https://fireballs.imo.net/members/imo/report_intro` since 2015. In 2019, 327 large events (with at least 10 reports) were submitted, a 14% rise with respect to the 287 such events in 2018. More event statistics, including a nice movie depicting where and when large fireball events took place since 2015, can be consulted at `https://fireballs.imo.net/members/imo_fireball_stats/`.

Observers were also treated to a short-lived α-Monocerotid outburst in 2019. Esko Lyytinen and Peter Jenniskens had predicted that the 2019 α-Monocerotids could behave in a similar way as in 1995, when a 40-minute outburst with ZHR reaching up to 400 was predicted and observed. Observations indicated that the predicted outburst was observed close to the predicted time, but rates were around 3–5 times lower than expected. Visual observers clearly observed an increase in activity, most of them recording 10 to 20 meteors in less than 30 minutes around $04^{\mathrm{h}}50^{\mathrm{m}}$–$05^{\mathrm{h}}00^{\mathrm{m}}$ UT, whereas activity was nearly nonexistent tens of minutes before and after.

New, powerful and easy-to-use data analysis software...

Since its foundation in 1988, IMO has strived to collect meteor observations and to distribute the results. In the past years, powerful tools have been developed to guarantee easy access to and analysis of visual and video data.

While preliminary automatic visual ZHR profiles can be consulted at `https://www.imo.net/members/imo_live_shower`, every single observation in IMO's Visual Meteor Database (VMDB) can be consulted and downloaded at `https://www.imo.net/members/imo_vmdb`. In the past years, Kristina Veljković has developed the powerful and easy-to-use visual meteor data analysis software MetFns. It is written in the statistical programming language R and can be freely downloaded from the CRAN webpage `https://cran.r-project.org/web/packages/MetFns/index.html`. Kristina has also developed the R shiny application MetFnsApp, which brings global analysis of visual meteor shower data within reach of everyone who is interested. The most elaborate part about analyzing visual meteor data is not how to use MetFnsApp, but selecting binning and other parameters in a clever and interactive way. This process is explicitly explained in

[1] Bogaertsheide 5, 2560 Kessel, Belgium.
Email: `cis.verbeeck@scarlet.be`

IMO bibcode WGN-481-verbeeck-janus NASA-ADS bibcode 2020JIMO...48....1V

(Rendtel et al., 2019a), where Jürgen Rendtel et al. demonstrate in detail how they went along to interpret and analyze the visual meteor data of the Perseids 2018. This paper describes the intermediate steps and iterations that were employed to derive the Perseid 2018 results in (Rendtel et al., 2019b).

2019 brought exciting news for video observers, when Sirko Molau introduced MeteorFlux 2.1 at the IMC 2019 in Bollmansruh (Molau, 2020). Apart from the introduction of several new functionalities into the MeteorFlux web tool, MeteorFlux 2.1 allows the user to select either the real-time view (updated every 5 minutes by MetRec, data not checked manually), the temporary view (data available after the observer has verified MetRec's meteor output), or the final view (checked by the observer and verified a second time with PostProc by an IMO network admin, backlog about 1 year). With MeteorFlux 2.1 you can plot the population index, ZHR, and flux of any shower and compare it to a selected reference shower (e.g., the sporadics or the average profile of the selected shower over several years) within a minute. Check it out at `https://meteorflux.org/`!

So please go ahead and write those articles!

With all these new data and tools at hand, do not shy away to produce your own analysis and share them with the meteor community through WGN or the IMO website. It goes without saying that WGN (`wgn@imo.net`) and the news editors of the IMO website (`newsitems@imo.net`) welcome all other kinds of meteor-related contributions as well!

Thank you

Megan Argo, Masahiro Koseki, Galina Ryabova, and Damir Šegon did not renew their mandate as Council members for the 2019 IMO Council elections. I want to thank them all for their valuable contributions as an IMO Council member during the past four years. I am happy to report that Francisco Ocaña Gonzalez and Vincent Perlerin were elected as new Council members for 2020–2023, and that Juraj Tóth and Javor Kac were re-elected for the same term. I am convinced they will bring new ideas and contributions to the IMO Council, to the benefit of our organization.

Needless to say, IMO's achievements and services are only possible through the dedication of many volunteers, such as WGN's Editor-in-Chief Javor Kac, our webmaster Karl Antier, and Mike Hankey and Vincent Perlerin who developed and maintain the IMO website, VMDB, and fireball form. Essential tasks are performed by the IMO Council members and Commission Directors and many more volunteers. Without mentioning them all in detail, I want to thank them all for their part in running the International Meteor Organization! Finally, I want to thank the LOC and SOC members of the IMC 2019 in Bollmansruh for having organized such a successful conference.

I wish you a healthy, happy, and exciting 2020 with clear skies and a lot of fireballs, and I hope to see you at the IMC in Hortobágy, Hungary on September 17–20!

References

Molau S. (2020). "MeteorFlux Reloaded". In *Proceedings of the International Meteor Conference 2019, Bollmansruh, Germany, October 3–6*. pages 57–59.

Rendtel J., Veljković K., Verbeeck C., Weiland T., and Knöfel A. (2019a). "Tricks of the trade: global analysis of visual meteor observations using VMDB and MetFns — an example". In *Proceedings of the International Meteor Conference 2018, Pezinok, Slovakia, August 30 – September 2*. pages 57–63.

Rendtel J., Veljković K., Weiland T., Verbeeck C., and Knöfel A. (2019b). "Perseids 2018 — analysis of global visual data". *WGN, Journal of the IMO*, **47:1**, 18–25.

Janus *was a Roman god with two faces, one looking to the past and one to the future, called upon at the beginning of any enterprise. Today he is often a symbol of re-appraisal at the start of the year.*

Letter — The CMN catalogue of orbits updated

Croatian Meteor Network [1]

After some delay, The Croatian Meteor Network has released its catalogues of orbits for 2014-2019. The catalogues can be accessed from the CMN download page:
`http://cmn.rgn.hr/downloads/downloads.html`

These are the last catalouges gathered by analogue cameras (Vida & Novoselnik, 2010; Gural & Šegon, 2010; Vida et al., 2014b) that were used by CMN until the middle of 2019. Since then, CMN has moved to a new mode of observing, using digital cameras and RPI computers with dedicated RMS software (Vida et al., 2018; Vida et al., 2014a).

The CMN Team.

References

Gural P. and Šegon D. (2010). "A new meteor detection processing approach for observations collected by the Croatian Meteor Network (CMN)". *WGN*, **37**, 28–32.

Vida D., , Zubović D., Šegon D., Gural P., and Cupec R. (2014a). "Open-source meteor detection software for low-cost single-board computers". In Roggemans A. and Roggemans P., editors, *Proceedings of the International Meteor Conference, Egmond, The Netherlands, 2016*. IMO, pages 59–63.

Vida D., Mazur M. J., Šegon D., Zubović D., Kukić P., Parag F., and Macan A. (2018). "A new meteor detection processing approach for observations collected by the Croatian Meteor Network (CMN)". *WGN*, **46**, 71–78.

Vida D. and Novoselnik F. (2010). "Croatian Meteor Network: data reduction and analysis". In Asher D. J., Christou A. A., Atreya P., and Barentsen G., editors, *Proceedings of the International Meteor Conference, Armagh, Northern Ireland, 2010*. IMO, pages 96–100.

Vida D., Šegon D., Gural P., , Martinović G., and Skokić I. (2014b). "CMN_ADAPT and CMN_binViewer software". In Rault J.-L. and Roggemans P., editors, *Proceedings of the International Meteor Conference, Giron, France, 2014*. IMO, pages 59–63.

IMO bibcode WGN-481-cmn-letter NASA-ADS bibcode 2020JIMO...48L...3C

[1] Email: `cmn@rgn.hr`

Radio meteors

A Head Echo Doppler Model for Assessment of Meteoroid Forward Scatter Characteristics

M. T. German [1]

A toy model has been developed to aid visualisation of forward scattered meteor head echo Doppler characteristics. A simplified geometry of a meteoroid entering the atmosphere has been used to determine the Doppler shift of the forward scattered signal during the head echo phase of the path. The meteoroid can be completely specified by its velocity in a Cartesian coordinate system and entry point in the region of space above the radio transmitter and receiver. Thus, by specification of speed, bearing and inclination relative to the receiver and transmitter, the meteoroid is tracked through a volume of space and the changing Doppler frequency calculated. The model is described in detail and the stages of development through to Monte Carlo simulations are described. Examples of simulations, including single paths and more complex randomisation of both single and multiple parameters are presented. Insight is provided into a complete distribution of Doppler shift frequencies and frequency slopes. A hitherto unrealised artefact from simulations uncovers a "no-go zone" for selected Doppler shifts.

Received 2019 December 22

1 Introduction

The paper "Whistling Meteors – A Doppler Effect Produced by Meteors Entering the Ionosphere" by two All India Radio engineers, Chamanlal & Venkataraman (1941)[a] was the first reported hearing of what are now known as "head echoes". They postulated that the changing audio tone arose solely from the deceleration of the meteor. Their ideas on the process causing the head echo were soon updated by Lovell et al. (1947), where it was generally agreed that the *"whistle should fall if the wave is scattered from the head of the meteor as it approaches [the radio transmitter/receiver] with constant velocity."* Over the nearly 80 years since those early reports, head echo measurement, theory and models have been fertile topics of study, yet the determination of Doppler characteristics pertinent to a given transmitter, receiver and meteoroid has hitherto been difficult for the amateur radio meteor observer to conceptualise.

The Head Echo Doppler Assessor (HEDA) toy model has been developed to aid the visualisation of forward scattered meteor head echo Doppler characteristics based on the velocity vector and entry point in the atmosphere relative to transmitting radio source and receiving observer. The term "toy" is used to describe its simplified geometry, simplifying assumptions and ease of use – a model to play with. It is not intended as an accurate "scientific" model although it may be developed in that direction. The models have been implemented, for convenience, using commercial software[b] which provides a built-in programming environment with data analysis and visualisation capabilities; the program scripts are compiled to give the necessary speed for the computationally intensive Monte Carlo simulations. However, the equations and algorithms are simple enough to be readily formulated in other programming languages.

The underlying assumption is that a meteoroid moves in the early part of path with a constant velocity and that generated ionisation (plasma) surrounding it remains spherical in shape thereby presenting a symmetrical target for isotropic radio wave scatter. Thus, the head echoes of all meteoroids illuminated by radio waves have the potential for detection within the scattered horizon.[c] Qualified substantiation of these and other assumptions are given in Section 3.

The process leading to a head echo at high altitudes is distinctly different to that at lower altitudes where the interaction with the denser atmosphere decelerates the meteor and a trail of slower ionisation stretching behind the meteor develops (Richardson & Kuneth, 1998). The specular scattering characteristics of these meteors are no longer isotropic and are not included in the present model. However, in a similar way that specular scatter from ionisation trails is critically dependent on the geometry of transmitter, meteor and receiver; it will be shown that the Doppler characteristics of meteoroid head echoes are governed exclusively by geometry and velocity.

The model uses a simplified geometry as shown in Figure 1 whereby the atmosphere is represented as a rectangular box above the transmitter (TX) and receiver (RX). The box contains the altitudes of interest and extends from the TX to RX and beyond and to either side of the of the TX-RX line.

All model meteoroid paths start at 120 km and end at 90 km altitude and can enter at any point through the

[1]Hayfield, High Peak, UK.
Email: mike.german@physics.org

IMO bibcode WGN-481-german-model
NASA-ADS bibcode 2020JIMO...48....4G

[a]Their paper is not generally available, but was noted in Nature (1942) and reviewed by Lovell et al. (1947) and later McKinley (1961). The McKinley text is also quoted in Richardson & Kuneth (1998).

[b]Igor Pro, WaveMetrics Inc., https://www.wavemetrics.com

[c]Received power and bandwidth will be limiting factors in detection.

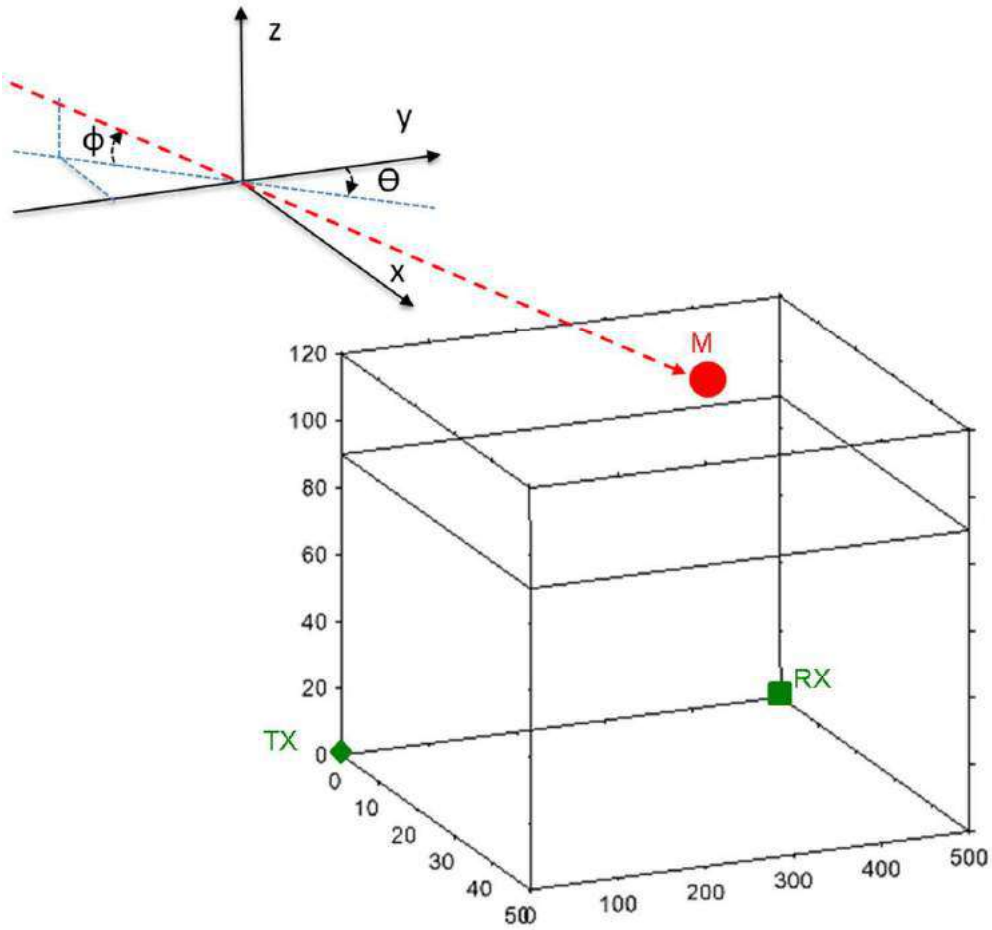

Figure 1 – Model geometry showing positions of Transmitter (TX), Receiver (RX) and Meteor (M). The angle of elevation is defined as Φ and the bearing as Θ. For clarity only positive axes are shown for the box.

top surface of the box. Cartesian coordinates are used with dimensions in km. The results in this paper have used, by way of example, the location and frequency of GRAVES[d] transmitter (TX) and the location of the author (RX), which is some 850 km in a generally NW direction from the GRAVES Dijon site.[e] However, the extent of the X, Y and Z axes can be set to any value. Thus the coordinates of TX are $x = 0$, $y = 0$ and $z = 0$, and RX are $x = 0$, $y = 850$ and $z = 0$. The modelled altitude of the atmosphere extends from $z = 90$ to $z = 120$, from the TX-RX ground plane. The meteor velocity vector is specified by magnitude, $|v|$, angle of elevation, Φ, and bearing, Θ. To simplify the model the bearing from TX towards RX is taken as $\Theta = 0°$ and $\Phi = 0$ corresponds to a horizontal direction. The path of the meteor is tracked in small steps of time during passage through the altitude layer, and the changes in range relative to TX and RX calculated. From this, using the bi-static Doppler equation[f], the Doppler shift is determined. Details of the geometry and methodology are given in Appendix A.

[d]No assumptions are made in this paper of GRAVES radiation pattern.

[e]For details of GRAVES see for example `http://www.fas.org/spp/military/program/track/graves.pdf` transmitter.

[f]The formulation given in `https://en.wikipedia.org/wiki/Bistatic_Doppler_shift` was used.

Head echo Doppler characteristics are governed by five variables: the meteoroid velocity vector components, $|v|$, Φ and Θ, and the rates at which the meteor moves toward or away from the transmitter and the receiver. However, in the model the range of the meteoroid from transmitter and receiver are determined from the X, Y and Z positions of the meteoroid. Since all model meteoroids start at $z = 120$ km and the positions of TX and RX are fixed, only the velocity vector components and the x and y entry coordinates are needed for the calculation.

2 Model results

2.1 Single Variable Simulations

The initial implementation of the model used fixed variables and a number of separate paths were calculated for comparisons of Doppler characteristics. Two simulations are shown in Figure 2a and 2b. The first simulation had fixed entry point, bearing and elevation angle and the velocity magnitude was varied in 6 steps. The second simulation was repeated with a different entry point.

The change in Doppler shift is evident along the individual velocity paths as is the variation with velocity and entry point. It will be noted that not all paths deliver a zero Doppler shift. This applies to the path down to an altitude of 90 km and may drop to that

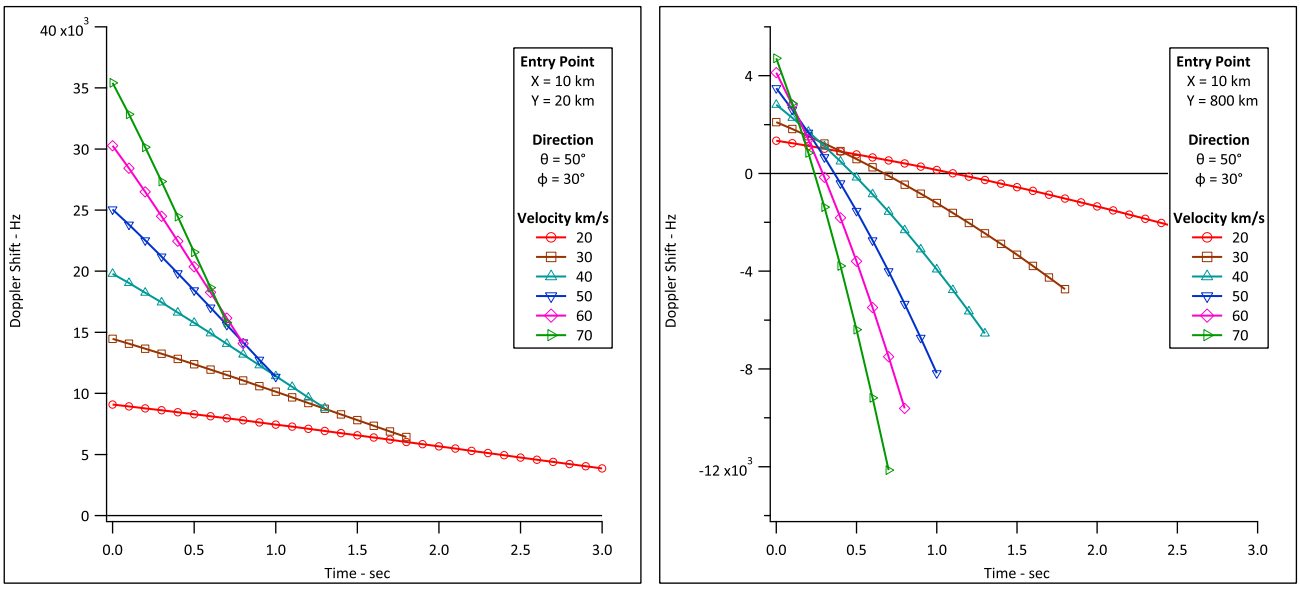

Figure 2 – The variation of Doppler frequency shift with time for model meteoroids with $|v|$ from 20 to 70 km/s. The elevation and bearing were fixed at $\Theta = 50^\circ$ and $\Phi = 30^\circ$. The plot on the left (a) is for an entry point into the atmosphere at $x = 10$ km, $y = 20$ km and plot on the right (b) for $x = 10$ km and $y = 800$ km. The frequency curves cover the time when the model meteoroid paths were between altitudes 120 to 90 km. Note the exponent of the values on the y-axes.

level at a later point of the path, but here, only the initial path is considered. The zero Doppler frequency is highlighted here because it is commonly recorded in monitor data. Other practical factors will, of course, affect the detectability of such frequencies by a radio meteor observer.

In these simple examples the Doppler shifts were found to vary from +36 kHz to −12 kHz. The frequency slope (rate of change of Doppler frequency) was also found to be dependent on initial conditions, and as indicated by the changing slopes in Figure 2b was not necessarily constant for the duration of the path.

2.2 Monte Carlo Approach

2.2.1 Introduction

It was realised that a better solution to the "single variable" approach of Section 2.1 was required to fully investigate the total range of possible Doppler shifts and frequency slopes. Therefore the model was extended to a Monte Carlo approach where one or more of the variables could be varied using random number generation. Usually each model meteoroid starts at a randomised point in XY model space at the maximum altitude Z. It is assigned a velocity vector comprising velocity magnitude, bearing and elevation, any of which may be fixed or randomised. The meteoroid is progressed down the path in fixed time steps, new positions being calculated from the previous position and the components of velocity along the X, Y and Z directions. From these changes in position, the range changes from TX and RX are calculated and the Doppler shift calculated (see Appendix A).

The velocity magnitude, bearing and elevation angle and the x and y positions for each path at the entry and exit points are stored. Also, at each step of path the calculated Doppler shift is compared against two test criteria to ascertain whether particular frequencies (for example zero Doppler shift) have been passed. If the criteria were met the corresponding altitude is stored for analysis.

Sufficient paths may be simulated to develop a reasonable picture of the Doppler characteristics: typically 20000 to 100000 random paths were used. The example simulations below are based on the GRAVES transmitter location (TX) and a receiver (RX) at a range of 850 km.

2.2.2 Monte Carlo Simulation 1 – All variables randomised

In simulation 1 the model had meteoroids passing through the maximum altitude X-Y area from any direction and elevation angle and with velocity magnitude between 20 and 80 km/s. Details are at Table 1 and all parameters were randomised. There were 20 000 random paths.

The distributions of Doppler frequency shifts at the 120 km entry surface and 90 km altitude surface are at Figure 3. The data were normalised to a percent-

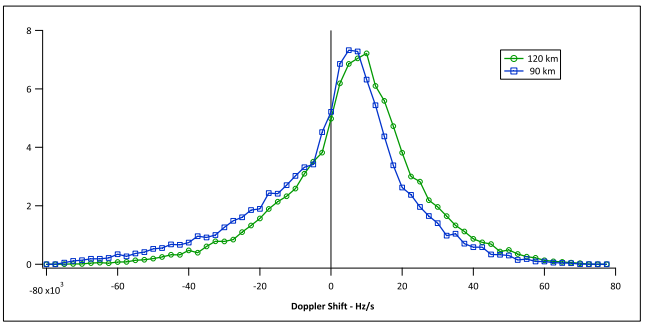

Figure 3 – Monte Carlo Simulation 1 – Distribution of Doppler frequency shifts as percentage of 20 000 randomised paths at the maximum (120 km) and minimum (90 km) altitudes. Note the 10^3 multiplying factor for the bottom axis values.

Table 1 – Limits of randomised parameters used in Monte Carlo Simulation 1.

Description	Parameter	Minimum	Maximum	Units
X range	x	-500	$+500$	km
Y range	y	0	1400	km
Velocity vector magnitude	$\|v\|$	20	80	km/s
Velocity vector bearing	Θ	0	360	degrees
Velocity vector elevation	Φ	0	90	degrees

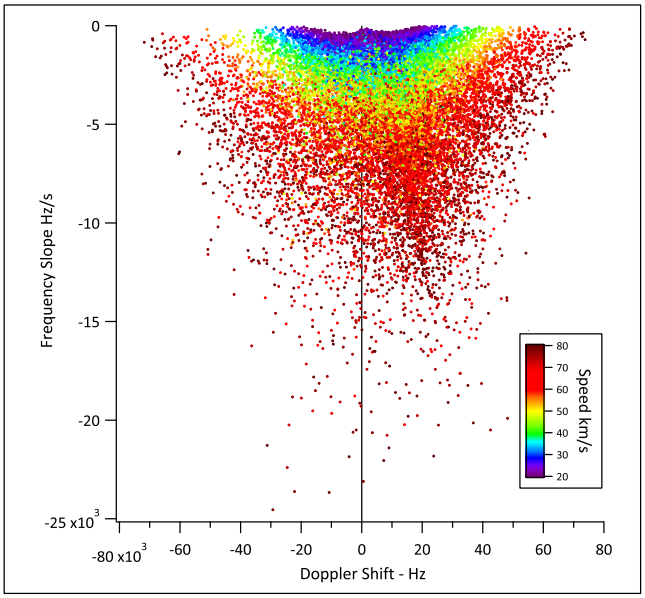

Figure 4 – Monte Carlo Simulation 1 – Variation of Frequency slope with Doppler Shift at the entry point surface.

age of the total number of randomised paths. The Doppler shift varied between ±80 kHz. There was a slight change of the distribution toward lower frequencies shifts as altitude reduced.

The Doppler shifts at the point of entry are plotted against frequency slope or rate of change of Doppler shift are shown in Figure 4. The slopes ranged from roughly −15 Hz/s to −25 kHz/s.

A test was also made along each of the paths to determine the altitude at which the Doppler shift passed through zero.[g] Roughly 10% of the random paths met this criterion.

This simulation essentially covered all possible meteoroids that could fall in the model space. Changes to the extent of the volume in the X and Y directions modified the statistics and shape of the plots. For example halving the X and Y dimensions resulted in a less smooth distribution curve and Doppler shifts between −30 kHz and +52 kHz at the entry altitude and −75 kHz and 43 kHz at the exit altitude. The frequency slopes were between roughly −200 Hz/s and −26 kHz/s.

2.2.3 Monte Carlo Simulation 2 – Fixed velocity magnitude, bearing and elevation angle

The model parameters were fixed to represent a meteor stream passing across and into the model space at a particular part of a shower. Arbitrarily the velocity magnitude was fixed at 30 km/s, the bearing at 45° and elevation at 30° and the XY entry points were randomised. The same entry area as the previous simulation was used. The values are at Table 2.

The distribution of Doppler shift frequencies is at Figure 5.

The range of Doppler frequency shifts spread either side of zero with a larger number in the negative region. The range was roughly between ±22 kHz. In addition to the highest number of paths at around −20 kHz, the distributions also shows peaks at about ±8 kHz.

An investigation of the distribution of Doppler frequency shift over the entry surface was achieved by a scatter plot of the individual start points in the XY plane and a colour used to indicate the corresponding Doppler shift as presented in Figure 6. All meteoroids had a bearing of 45° corresponding in the Figure to paths parallel to a 45° line from $x = -500$ and $y = 0$. A "red shift" can be seen for paths beyond TX and RX as meteoroids moved away.

A similar scatter plot was constructed for the frequency slope, shown as Figure 7, where the colour now represents the rate of change of the Doppler frequency or frequency slope. The frequency slope varied between −500 Hz/s to 3.5 kHz/s. Rapid changes in the Doppler frequency slope around the TX and RX points where the slopes become steeper as evidenced by the closeness of the colour changes.

2.2.4 Monte Carlo Simulation 3 – Fixed velocity magnitude and elevation, and randomised bearing

In Section 2.1 it was seen that the Doppler shift did not reach zero for all paths. This was investigated

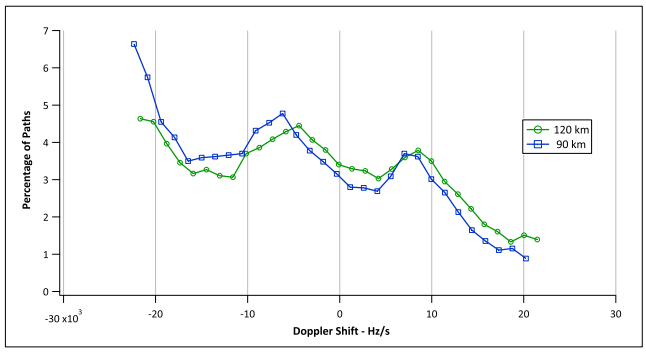

Figure 5 – Monte Carlo Simulation 2 – Distribution of Doppler frequency shifts as percentage of 20 000 paths. The simulation had fixed velocity magnitude, bearing and elevation. The curves are at the entry surface (120 km) and exit surface (90 km) altitudes. Note the 10^3 multiplying factor for the bottom axis values.

[g] A window of ±1 Hz was used for the test.

Table 2 – Randomised and fixed parameters used in Monte Carlo Simulation 2.

Description	Parameter	Minimum	Maximum	Units
X range	x	−500	+500	km
Y range	y	0	1400	km
Velocity vector magnitude	$\|v\|$	30		km/s
Velocity vector bearing	Θ	45		degrees
Velocity vector elevation	Φ	30		degrees

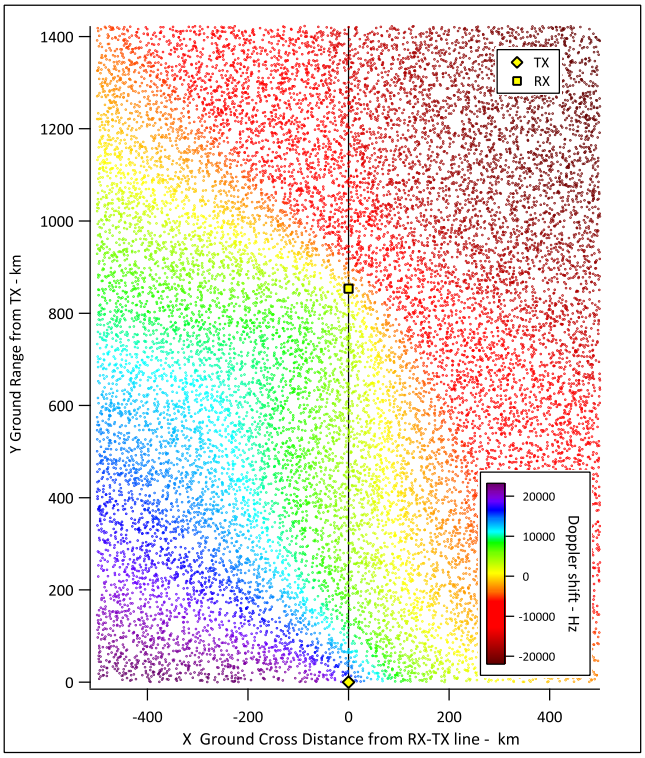

Figure 6 – Monte Carlo simulation 2 – The variation of Doppler frequency shift with entry point.

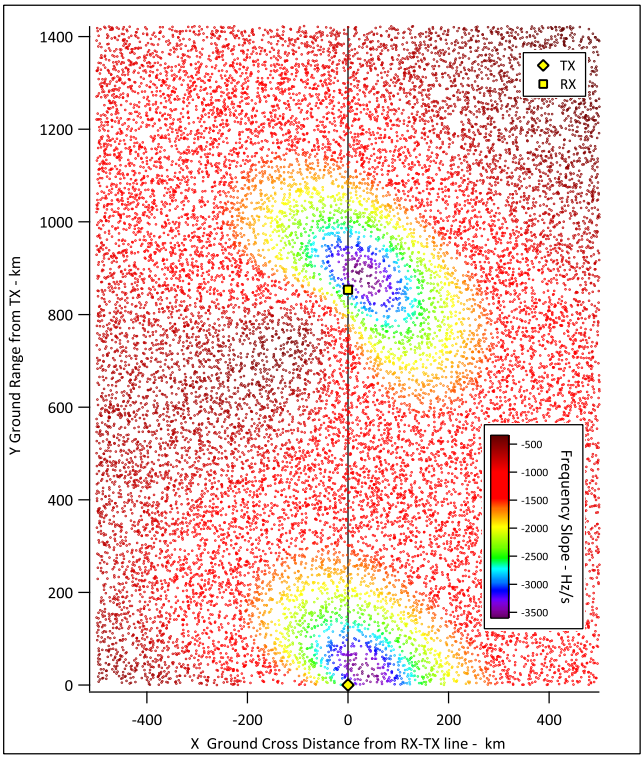

Figure 7 – Monte Carlo simulation 2 – The variation of frequency slope with entry point.

further using the test criteria approach mentioned in Section 2.2.1. Previous simulations had found that less than 10% of paths met the "zero Doppler" criterion and consequently 100 000 randomised paths were needed. Two Doppler shift tests were made, one for 0 Hz and the other for 2000 Hz.[h] The velocity magnitude and elevation angle were fixed and entry points randomising as detailed in Table 3.

For this simulation 7% of the paths met the criteria. The results are shown in the scatter plots of Figures 8a, 8b and 8c. Figure 8a shows the entry points of the paths meeting the zero Doppler shift criteria and 8b shows for these paths the altitudes at which zero Doppler shift was passed. Figure 8c is for the entry points meeting the 2000 Hz criteria.

Generally there appears to be a fairly uniform spread in points with an increasing concentration around an oval region where no paths met the criteria. For the zero Doppler shift criterion a "no-go zone" extends in the X direction 150 km either side of the TX-RX line and, in the Y direction to beyond the TX and RX. In an XYZ view (not shown here) of the points in Figure 8b there appeared to be a sharp sided oval shaped cylinder extending vertically from the entry altitude down to the exit altitude. It should be remembered that the elevation angle was 60° and therefore the steepness of the sides are not those of the meteoroid path. A similar, but differently shaped, no-go zone was seen for the 2000 Hz criterion data.

[h] Acceptance windows ±1 Hz on these frequencies were used in the model.

Table 3 – Randomised parameters used in Simulation 3.

Description	Parameter	Minimum	Maximum	Units
X range	x	−500	+500	km
Y range	y	0	1400	km
Velocity vector magnitude	$\|v\|$	20		km/s
Velocity vector bearing	Θ	0	360	degrees
Velocity vector elevation	Φ	60		degrees

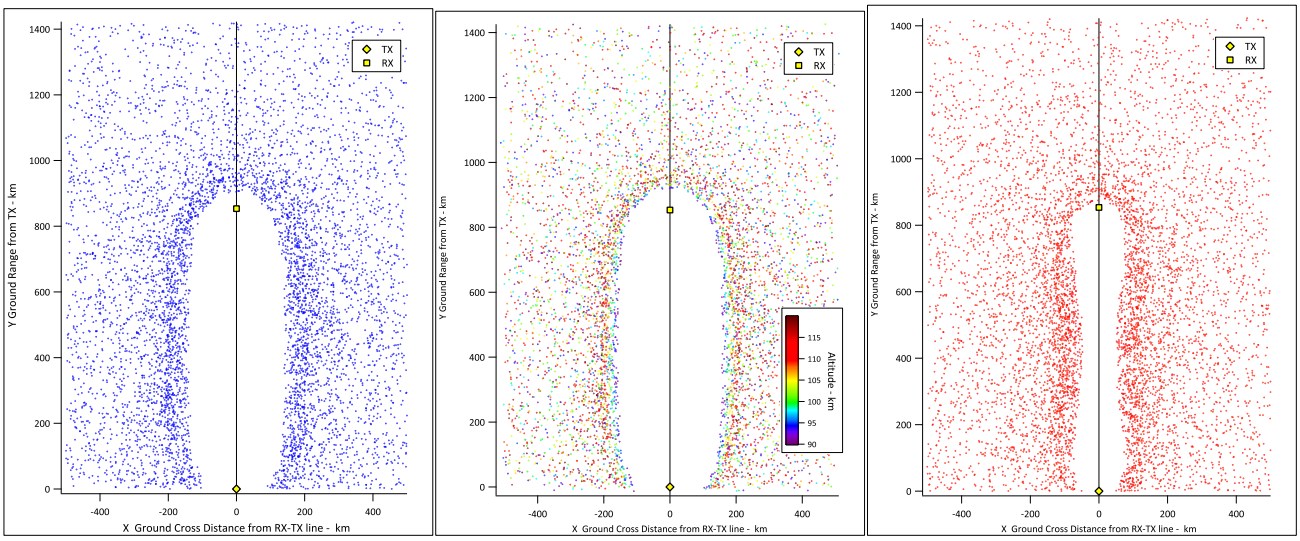

Figure 8 – Monte Carlo Simulation 3 – left (a): Distribution of paths at the entry point surface meeting the "zero Doppler" criterion; middle (b): Distribution of paths at the altitude meeting the "zero Doppler" criterion. The colour indicates the altitude; right (c): Distribution of paths at the entry point surface meeting the 2000 Hz criterion.

The shape and size of the no-go zone varied with velocity magnitude and elevation angle.

3 Discussion of Assumptions

3.1 Isotropic scatter

A search of the literature found the following example comments supporting isotropic scatter in the head echo region as a reasonable approach.

From the head echo measurements with the Scandinavian EISCAT[i] radars, Kero et al. (2008) concluded *"... RCS is close to isotropic ... consistent with an essentially spherical target as first measured by Close et al. (2002a) during the Leonid 1998 storm.*

Radio meteor head echoes polarisation measurements were conducted by Wannberg et al. (2011) using a tristatic UHF radar. They made use of the Dyrud et al. (2008) model and found that the majority of head echoes observed by them appear to be from meteoroid targets that were isotropic in backscatter. They concluded that *"head echo events can in general be safely assumed to represent isotropic scatterers..."*

Kero et al. (2013) state that meteor head echoes arise from scattered radio waves from the dense plasma surrounding and co-moving with a meteoroid and Close et al. (2015) combine several theoretical models to develop a new model for scattering from an assumed spherical head plasma.

3.2 Altitude Range

Examples from the literature, describing head echo altitudes are below.

A plasma and electromagnetic model of head echoes was developed by Dyrud et al. (2008) to address "the poorly understood radio scattering characteristics of the meteor plasma." The head echo region was described as an "ablation and ionization stage." At later stages between 115 and 90 km they showed a "cooled trail plasma" column that reduced in radius with altitude.

[i]European Incoherent Scatter

In a review of radar meteor studies at the Arecibo Observatory, Mathews et al. (2003) stated *"As the head-echo only develops in the 80–130 km altitude 'meteor zone' it is also clear that the head echo results from radar scattering from the 'plasma' that develops around the meteoroid as it interacts with the atmosphere."*

Westman et al. (2004) investigated head echo altitude distributions using UHF and VHF systems. They determined altitude limits, dependent on meteoroid size and velocity between 80 and 125 km.

3.3 Constant Velocity

Dyrud et al. (2008) in their Figure 1 gives a clear example of a constant velocity head echo alongside a slightly later non-specular trail "reflection". The head echo is evident between 105 and 95 km altitude.

Richardson and Kuneth (1998) noted in their head echoes measurements of Leonids, small reductions in velocity during a 178 ms period of 68.3 down to 67.1 km/s (equivalent to 6.7 km/s/s) and over a 315 ms period 64.0 down to 62.3 km/s (5.5 km/s/s). They were unable to state the altitudes where these changes occurred.

The measurements of Close et al. (2002b) found the highest decelerations were at 104 km with most less than 50 km/s/s and several greater than 100 km/s/s.

Verbatim from Li (2019) *"The reduction in velocity at 105 km from the highest altitude of observation [stated earlier in their paper as 140 km] is less than 1 km/s, which is also supported by calculations based on momentum equation for a meteoroid mass of* 10^{-13} *kg. Reduction in velocity from 105 to 99 km is about 3 km/s for a meteor descending at 60 km/s but negligible for a meteor descending at 20 km/s. Atmospheric drag has minimum effect on half of the meteors observed above 105 km. It is possible that atmospheric drag may have a significant effect for meteors observed below 95 km, but their number is relatively small (5.5%)."*

4 Conclusions

A simplistic model of head echo Doppler scatter characteristics has been described in detail and some examples simulations presented. The assumption of isotropic scatter is supported by the literature referenced in Section 3. The altitude range chosen for simulations is within the generally accepted bounds. It is perhaps most difficult to be definitive with regard to constant velocity; deceleration, if any, was shown form literature to depend on meteoroid size, velocity and altitude. Nevertheless, for a simplistic model the assumptions are acceptable.

The sample simulations here were based on the location and frequency of GRAVES TX and the location of the author's RX. Other wavelengths and configurations may be readily calculated using the same methodology and algorithms.

From the simulations using only the TX, meteoroid and RX positions and meteoroid velocity some interesting and perhaps significant data has been generated.

The results for Doppler shift frequency distribution were found to be dependent upon the X and Y limits used in the simulation. Although a better knowledge of the sky illuminated by the rear/side lobes of GRAVES would undoubtedly improve the overall value of results, the distributions of Doppler shift remain useful in scoping exercises for head echo frequency measurements. For example from Figure 3 the sampling rates and frequency bandwidth of receiving and recording equipment could be designed to capture frequency slopes of up to, say -15 kHz/s; or the bandwidth expanded to accommodate frequencies between, say, ± 20 kHz; or optimisation conducted based on the highest probabilities.

The simple representation of a meteor stream in the second simulation (Section 2.2.3) generated interesting features in the Doppler shift and frequency slope scatter plots, associated with the TX and RX. They are worthy of further study, perhaps through comparison with head echo measurements with the optimistic aim of identification of location or direction.

The emergence of the "no-go zone" artefact (Section 2.2.4) from such a simple model was surprising. Whereas all meteor produce a Doppler shift, only a small fraction have paths that include zero shift. Thus, for certain meteor situations a volume of space can exist where no meteors reach zero Doppler shifts and an apparent no-go-zone exists. It is believed to be real effect that should be evident in radio monitoring results.

The model will hopefully be developed and extended by others. The author intends further developments, for example incorporation of the ideas and geometry of Verbelen (2019). It is also hoped that head echo meteor data collection as developed by Kaufmann (2017) will be developed to enable study of the more exotic features uncovered in this paper.

Acknowledgements

Thanks are extended to Jean-Louis Rault for his encouragement to complete this paper. I am indebted to Wolfgang Kaufmann for his wise advice, our discussions and for his critical reading and comments on the final draft. Finally, and not in the least, to Lesley my wife, for enduring the many hours spent developing, playing with and writing about my toy model, and for the unending mugs of tea without which nothing would have been possible.

References

Chamanlal and Venkataraman K. (1941). "Whistling meteors - a doppler effect produced by meteors entering the ionosphere". *Electrotechnics (Bangalore, India)*, **14**, 28–40. (Summary in "Whistling Meteors" (1942). Nature **149**, 416-417.).

Close C., Oppenheim M., Durand D., and Dyrud L. (2015). "A new method for determining meteoroid mass from head echo data". *Journal of Geophysical Research*, **110**, 1–6.

Close S., Hunt S., and McKeen F. (2002a). "Characterization of Leonid meteor head echo data collected using the VHF-UHF Advanced Research Projects Agency Long-Range Tracking and Instrumentation Radar (ALTAIR)". *Radio Science*, **37:1**, 1–9.

Close S., Oppenheim M., Hunt S., and Dyrud L. (2002b). "Scattering characteristics of high-resolution meteor head echoes detected at multiple frequencies". *J. Geophys. Res.*, **107:A10**, 1295.

Dyrud L., Wilson D., Boerve S., Trulsen J., Pecseli H., Close S., C. C., and Lee Y. (2008). "Plasma and electromagnetic simulations of meteor head echo radar reflections". *Earth, Moon, and Planets*, **102**, 383–394.

Kaufmann W. (2017). "New radio meteor detecting and logging software". *WGN, Journal of the IMO*, **45:4**, 67–72.

Kero J., Szasz C., and Nakamura T. (2013). "MU head echo observations of the 2010 Geminids: radiant, orbit, and meteor flux observing biases". *Ann. Geophys.*, **31**, 439–449.

Kero J., Szasz C., Wannberg G., Pellinen-Wannberg A., and Westman A. (2008). "On the meteoric head echo radar cross section angular dependence". *Geophysical Research Letters*, **35**, L07101. doi:10.1029/2008GL033402.

Li Y. (2019). "A Study on Meteor Echoes Using the Arecibo and Jicamarca High Power Large Aperture Radars". Master's thesis, Miami University.

Lovell A., Prentice J., Porter J., Pearse R., and Herlofson N. (1947). "Meteors, comets and meteoric ionization". *Rep. Prog. Phys.*, **11**, 389–454.

Mathews J., Doherty J., Wen C.-H., Briczinski S., Janches D., and Meisel D. (2003). "An update on UHF radar meteor observations and associated signal processing techniques at Arecibo Observatory". *Journal of Atmospheric and Solar-Terrestrial Physics*, **65**, 1139–1149.

McKinley D. (1961). *Meteor Science and Engineering.* McGraw-Hill, New York. pp 17.

Richardson J. and Kuneth W. (1998). "Revisiting the radio doppler effect from forward-scatter meteor head echoes". *WGN, Journal of the IMO*, **26:3**, 117–130.

Verbelen F. (2019). "Meteor velocity derived from head echoes obtained from a single observer using forward scatter from a low powered beam". *WGN, Journal of the IMO*, **47:2**, 49–54.

Wannberg G., Westman A., and Pellinen-Wannberg A. (2011). "Meteor head echo polarization at 930 MHz studied with the EISCAT UHF HPLA radar". *Ann. Geophys.*, **29**, 1197–1208.

Westman A., Wannberg G., and Pellinen-Wannberg A. (2004). "Meteor head echo altitude distributions and the height cutoff effect studied with the EISCAT HPLA UHF and VHF radars". *Annales Geophysicae*, **22**, 1575–1584.

Handling Editor: Jean-Louis Rault

Appendix A. Head Echo Doppler Assessor (HEDA) Model Details

The Head Echo Doppler Assessor (HEDA) model geometry uses Cartesian coordinates and an example is

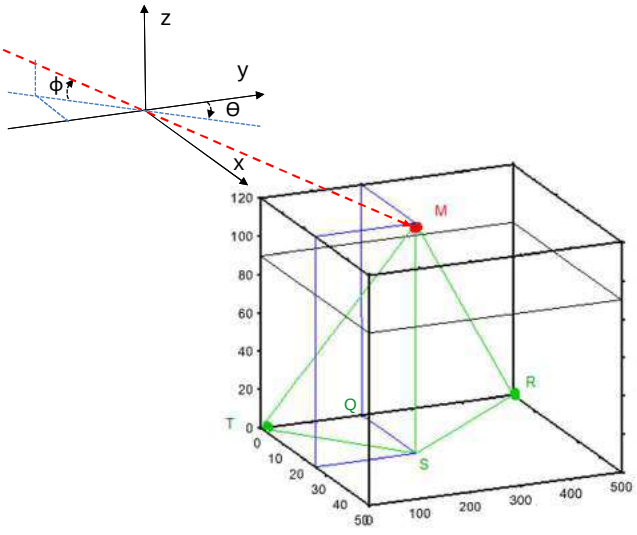

Figure A1 – Model Geometry.

The coordinates of transmitter T are $X_T = 0$, $Y_T = 0$ and $Z_T = 0$ and the receiver R, in this example, $X_R = 500$, $Y_R = 0$ and $ZR = 0$. Here, a meteoroid, M, has the coordinates $X_M = 20$, $Y_M = 200$ and $Z_M = 120$. The point S is at $X_S = 20$, $Y_S = 200$ and $Z_S = 0$ and vertically below M and the point Q is at $X_Q = 0$, $Y_Q = 200$ and $Z_Q = 0$. The positions of S and Q are used in the calculations.

The meteor velocity is specified by magnitude, $|v|$, angle of elevation, Φ, and bearing from the TX-RX line, Θ and shown in the top left of Figure A1. The velocity is resolved in Cartesian coordinates as,

$$V_x = |v| * \cos\Phi * \sin\Theta,$$
$$V_y = |v| * \cos\Theta * \cos\Phi,$$
$$V_z = |v| * \sin\Phi.$$

The Doppler shift, ΔDopp, for a wave scattered by a moving object with separated transmitter and receiver is given by,

$$\Delta\text{Dopp} = \frac{1}{\lambda}\frac{d}{dt}(R_{\text{TM}} + R_{\text{MR}}) \tag{1}$$

where λ is the transmitted wavelength, $\frac{d}{dt}(R_{\text{TM}}+R_{\text{MR}})$ is the rate of change of the transmitter to meteoroid range plus the rate of change of the meteoroid to receiver, R_{TM} is the range the transmitter T from the meteoroid M from and R_{MR} is the range of the meteoroid M from the receiver R. The meteoroid is advanced along a given path in time step dt.

From Figure A1, R_{TM} is the length of the line between points T and M and is calculated from triangles TMS and TQS as given by equation (2),

$$R_{\text{TM}} = (X_{\text{M}}^2 + Y_{\text{M}}^2 + Z_{\text{M}}^2)^{\frac{1}{2}} \tag{2}$$

Similarly R_{MR}, is calculated from QRS and R_{SM} from equation (3),

$$R_{\text{MR}} = (X_{\text{M}}^2 + (Y_{\text{R}} - Y_{\text{M}})^2 + Z_{\text{M}}^2)^{\frac{1}{2}} \tag{3}$$

As the meteor passes through the upper atmosphere X_{M}, Y_{M} and Z_{M} are calculated at each new position $n, n+1\ldots$

$$X_{\text{M}_{n+1}} = X_{\text{M}_n} + V_x * dt \tag{4}$$
$$Y_{\text{M}_{n+1}} = Y_{\text{M}_n} + V_y * dt \tag{5}$$
$$Z_{\text{M}_{n+1}} = Z_{\text{M}_n} - V_z * dt \tag{6}$$

where t_n and t_{n+1} are consecutive steps and the time step $dt = t_{n+1} - t_n$. From equations (4), (5) and (6) new values of R_{MR} and R_{TM} are calculated, and hence, by substitution of equations (4), (5) and (6) in equations (2) and (3) the value of $\frac{d}{dt}(R_{\text{TM}} + R_{\text{MR}})$ is determined from equation (7).

$$\frac{d}{dt}(R_{\text{TM}}+R_{\text{MR}}) = \frac{(R_{\text{TM}_{t_{n+1}}} - R_{\text{TM}_{t_n}}) + (R_{\text{MR}_{t_{n+1}}} - R_{\text{MR}_{t_n}})}{t_{n+1} - t_n} \tag{7}$$

The Doppler shift ΔDopp, equation (1), is then calculated and a new time step started. The model terminates when the altitude of the meteor, Z_{M}, drops to the lower specified altitude.

The rate of change of Doppler shift (frequency slope) is calculated from $\frac{d}{dt}(\Delta\text{Dopp}) = (\Delta\text{Dopp}_{n+1} - \Delta\text{Dopp}_n)/dt$.

Limitations of the observability of radio meteor head echoes in a forward scatter setup

Wolfgang Kaufmann [1]

During the maximum activity of the Quadrantids in 2018 a forward scatter radio observation failed to detect head echoes of this stream for more than one hour. A simulation of head echo Doppler shifts was performed on the basis of fixed receiver-transmitter-geometry with varying meteoroid trajectories in the height of 120–80 km. It could be shown that the ascertained head echo blackout coincided with a radiant position of the Quadrantids that resulted in trajectories producing very large Doppler shifts. From forward scatter radio observations it was found that the signal strength of a head echo declines rapidly with increasing Doppler shift. Simple forward scatter radio systems usually are too insensitive to detect head echoes Doppler shifts above a few kHz when meteoroid masses are small. This caused the blackout.

Received 2019 December 23

1 Introduction

The radio observation of meteors is possible via the reception of radio waves having been forward scattered off ionized meteor trails as well as off the small intense plasma region surrounding the meteoroids itself during their atmospheric passage between 140 and 70 km height. The latter scattering-type is called meteor head echo. Kero et al. (2008b) detected head echoes at aspect angles all the way out to 130° from the direction of meteoroid propagation (a further extension of the aspect angle was limited by the antenna pointing directions in their tristatic radar system). Thereby they found the radar cross section to be close to isotropic in the whole observable range, consistent with an essentially spherical target as first measured by Close et al. (2002).

The radio observation of such approximately isotropically scattering spheres theoretically should be possible from any position on the earth as long as they are above the horizon. The observability of head echoes is limited by the radar cross section of the meteoroid and the power of the transmitter in combination with the sensitivity of the receiver. The radar cross section mainly depends on the mass of the meteoroid, its velocity and height and on the frequency (Close et al., 2002).

On its flight a meteoroid shows a permanent changing radial velocity with respect to the observer (Kero et al., 2008a). In consequence the frequency of the head echo shows a continuously changing Doppler shift. E.g. during a radio observation of a fireball Rault et al. (2017) recorded an initial Doppler shift of 47 kHz continuously falling to zero Hz. From the radio observation of forward scattered head echoes the signal strengths of head echoes were found to decline rapidly with increasing Doppler shift (e.g. Kaufmann (2018), Fig. 2) So with smaller meteoroids only Doppler shifts of a few kHz can be observed with a basic receiving system. German (2020) showed in his simulation that there exists a number of trajectories resulting in very large Doppler shifts. These are far beyond the capability of a basic receiving system. So not all small meteoroids above the horizon deliver receivable head echoes. Their radio observability depends on the receiver-transmitter-trajectory geometry.

In the light of this finding the radio observation of the Quadrantids (QUA) 2018 were reexamined. During the maximum of activity not a single meteor head echo could be observed from Algermissen, Northern Germany for more than one hour. However trail reflections were present. No explanation has been found for this phenomenon so far. Now it may be explained by meteoroid trajectories resulting in unobservable large Doppler shifted frequencies. It is the aim of this paper to verify this hypothesis.

2 Material and Methods

A python script "MDopplerShift"[a] has been written to implement a bistatic radar model for calculating Doppler shifts. It was build on the thesis of Thomson (1985). The bistatic model bases on Cartesian coordinates. The origin of the coordinate system is coincident with the receiver position ($x = 0, y = 0, z = 0$). The transmitter is positioned at a distance D on the x-axis ($x = D, y = 0, z = 0$). The meteoroid is entering the scene anywhere in the space (x, y, z). Its bearing is indicated counterclockwise as angle between its forward direction and the receiver⇒transmitter direction (= baseline). Its inclination is specified as angle towards horizon. The meteoroid progress is stepwise calculated from its entry point. The Python script allows for the calculation of multiple trajectories from an entry point by automatically changing inclination and bearing in arbitrary steps. For further analysis the time-, x-, y-, z- and Doppler shift- data of the simulated trajectories were stored as csv-file. The further analysis was performed by a spread sheet program.

The radio registration of meteor reflections during the active period of the QUA 2018 took place in Algermissen, Northern Germany. The French radar-transmitter GRAVES was employed for forward scattering. It transmits a continuous rf-signal at a frequency of 143.050 MHz and illuminates a defined volume in the sky over southern France. A HB9CV-antenna, the SDR-receiver Funcube Dongle Pro+[b], the SDR-software

[1]Lindenweg 1e, 31191 Algermissen, Germany.
Email: contact@ars-electromagnetica.de

IMO bibcode WGN-481-kaufmann-observability
NASA-ADS bibcode 2020JIMO...48...12K

[a] http://www.ars-electromagnetica.de/robs/download.html
[b] http://www.funcubedongle.com/

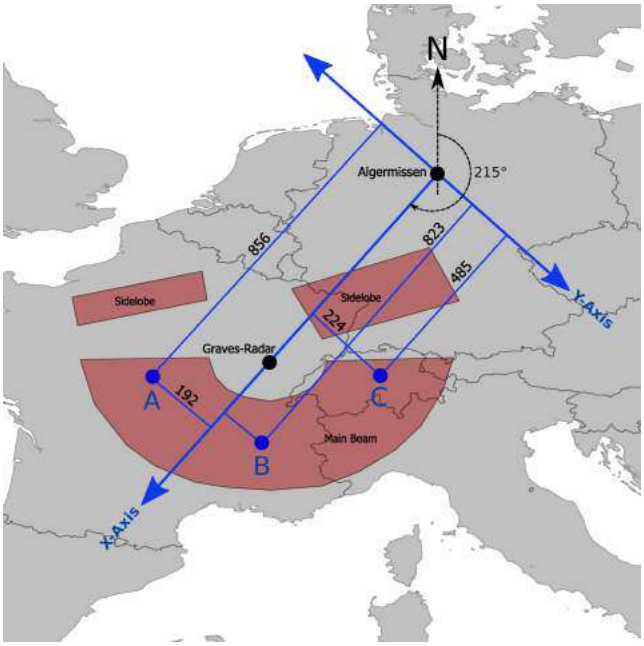

Figure 1 – Map of the receiver- and transmitter-positions. The GRAVES-radar illuminates a defined volume in the sky. A cross section in 100 km height is indicated (Kaufmann, 2018). Three meteoroid entry points, A-C, are chosen as representatives for all meteroroids entering the main beam. The x- and y-distances are indicated related to the receiver position. The distance between Algermissen and the transmitter is about 640 km. The azimuth of the receiver⇒transmitter baseline is about 215°. Map made with Natural Earth in the WGS 84 coordinate system.

SDR#[c] and the meteor-registration-software MeteorLogger[d] (Kaufmann, 2017) were used. The extraction of head echoes from the multitude of received signals and the computation of their frequency slopes was done by ProcessData[d]. Also ProcessData calculated the diurnal course of the QUA radiant in terms of azimuth (from north clockwise) and altitude from the given celestial coordinates at the time of maximum activity (Rendtel, 2017). For the head echo analysis the method of kernel density mapping was employed (Kaufmann, 2018), which is based on frequency slopes.

The trajectories of meteoroids originating from a radiant at azimuth, $AZ_{radiant}$, are orientated towards the observer and have therefore a reversed azimuth, $AZ_{meteoroid} = AZ_{radiant} + 180°$. The relation between the bearing of a meteoroid which is referenced to the baseline and its azimuth which is referenced to true North is $AZ_{meteoroid} = AZ_{baseline} - Bearing_{meteoroid} + 360$.

The extraction of head echoes of the QUA on base of the kernel density map was done by QGIS[e]. The head echo table can be imported in QGIS, using decimal date and log|slope| as x- and y-coordinates.

3 Results and Discussion

To get an idea which trajectories from which entry points can be recorded theoretically at Algermissen three representative entry points, A-C, were adopted in the main beam of GRAVES, see Figure 1. For each of this three entry points different trajectories were calculated by decreasing inclination from 0° to −90° in 5° steps and increasing bearing from 0° to 350° in 10° steps. Thereby progress of the meteoroids always was calculated in 100 ms steps. The geocentric velocity of incoming meteoroids was set to 40 km/s, the transmitter frequency to 143 050 000 Hz and the height z of the entry points to 120 km. The run time of the simulations was set to 5 s because of the finite extent of the illuminated sky volume. Figure 2 shows the graphical result of the simulation for entry point B. Obviously there exist a large number of trajectories that produce very large Doppler shifts in the given circumstances.

The existing, presumably numerous, back lobes of GRAVES were not taken into account, because their radiated power is much lower compared to the power of the main beam. Referred to the receiving system in use their contribution to the number of recorded head echoes is very small.

To adapt the outcome of the simulation to the capability of the used receiving system the data set was reduced to segments of trajectories which produce Doppler shifts running through zero Hz within a height of 120–80 km. From these segments the track points being closest to zero Hz Doppler shift were selected and their bearing/inclination-combinations were plotted, see Figure 3. The gaps between entry points A, B and C should be closed in real life by further entry points between A, B and C. So there remains a prominent gap centered around 200° bearing and a much smaller gap centered around 30° bearing. This would mean at Algermissen radio records at least do not include head echoes from meteoroids originating from southern radiants with an azimuth of around 195° and from northern radiants with an azimuth of approximately 5° if having a geocentric velocity of 40 km/s. The existence of such gaps were described by German (2020) as "no-go-zones."

Remarkable is that for a given bearing and inclination predominantly only one of the three entry point delivers head echoes with zero Doppler shifts (Figure 3). So for any bearing/inclination only a small part of the main beam reflects receivable head echoes towards Algermissen. This may additionally explain why the number of received head echoes in the radio measurements of Kaufmann (2018) were only about 10% of the number all signals. Hitherto this fraction was assumed to be only a matter of radar cross section of the incoming meteoroids.

The prediction of excluded head echo reception were verified by a radio observation of the head echoes of the Quadrantids 2018 (geocentric velocity about 41 km/s (Rendtel, 2014)). During the shower's maximum activity its radiant run through the above mentioned 5° azimuth gap. Figure 4 shows the kernel density map of all recorded head echoes from 2018 January 1 to 5. The QUA can be seen as prominent hot spot around January 4. Interestingly at the forecasted time of maximum activity January 3, 22^h UTC (Rendtel, 2017) over a span of more than one hour there was not a single head echo

[c] https://airspy.com/download/
[d] http://www.ars-electromagnetica.de/robs/download.html
[e] https://www.qgis.org

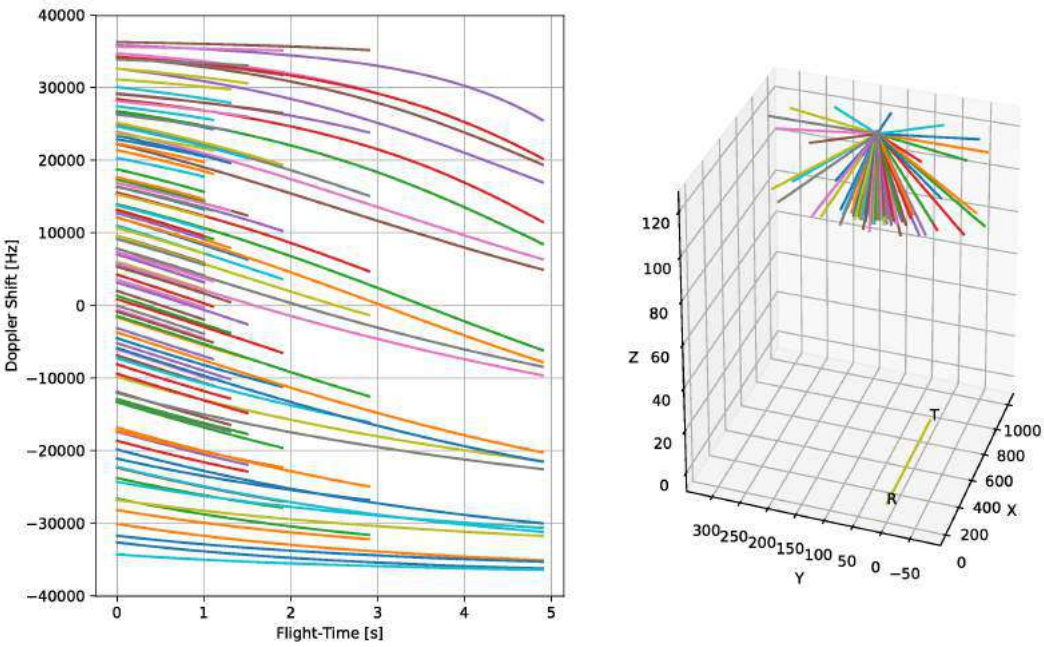

Figure 2 – The left plot is a graphical representation of the Doppler shifts produced by a meteoroid entering at point B (see Figure 1) with varied inclinations (10° steps) as well as bearings (30° steps). The right plot visualizes these different trajectories related to the receiver⇒transmitter baseline. The height is limited to a range of 120–80 km.

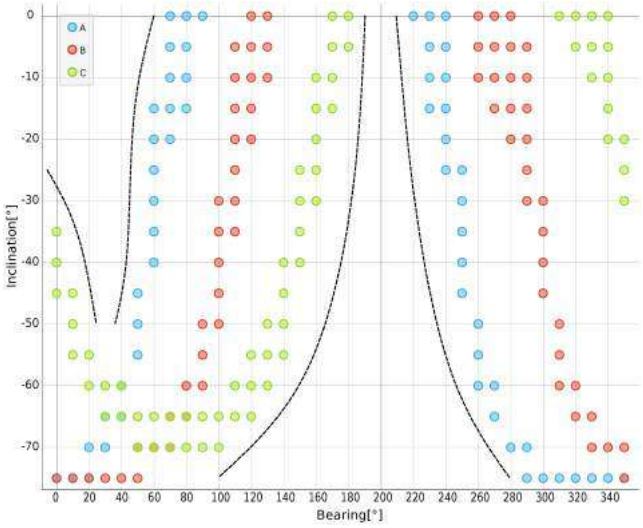

Figure 3 – Bearing-/inclination-combinations of track points close to zero Hz Doppler shift extracted from trajectories starting from the entry points A (blue), B (red) and C (green). Two gaps became apparent and were marked by dotted lines.

within the QUA hot spot registered. However trail reflections as well as head echoes of sporadic meteors were recorded. So this phenomenon was not due to a shutdown of the receiving system (as it was from January 3, 09^{h}–14^{h} UTC) or the very low altitude of the radiant at this point of time.

To analyse this further the QUA head echoes were extracted from the kernel density map by selecting all signals within the QUA hot spot. By this approach a small contribution of sporadic meteors of the apex source to the QUA could not be avoided in the period 03^{h}–06^{h} UTC because of the rather similar log|slopes| of both, see Figure 4. The QUA signals were summarized to hourly count rates (HCR). Mean hourly altitude is used for zenithal correction of the HCR [ZHR_r = HCR/ sin(altitude)] according to Rendtel et al. (2016). For a better comparability with Figure 3 the hourly means of azimuth and altitude of the QUA-radiant were converted to bearing and inclination of its meteoroids. Now the ZHR_r of the QUA head echoes were plotted in a bar chart together with the course of bearing and inclination of the QUA-meteoroids, see Figure 5. A progressive decline to 0 in the ZHR_r can be seen from 20^{h}–22^{h} UTC followed by a hesitant recovery of ZHR_r until 0^{h}. Within this time span the bearing moved from 30° down to 355° and inclination changed from −4° to −20°. Looking at Figure 3 all these combinations are lying completely within the gap centered around 30° bearing. The observed depletion of ZHR_r is not centered around 30° bearing but around 12°. However, considering that the sky illumination of GRAVES radar is an approximation derived from a few pieces of information and effects of meteoroid deceleration as well as curvature of the earth are not considered, the congruence between simulation prediction and real observation is remarkably well.

4 Conclusion

Although meteoroids are coated with an almost spherical plasma sheath from about 140 km down to 70 km height which should scatter incident radiation generally isotropically their head echoes are not observable in all case. Incoming meteoroids can have trajectories resulting in very large Doppler shifts in a forward scatter observation which make them unrecognisable to a basic receiving system. This effect not only modulates the number of recorded head echoes itself but also may prevent the coincident registration of a common meteoroid from different sites.

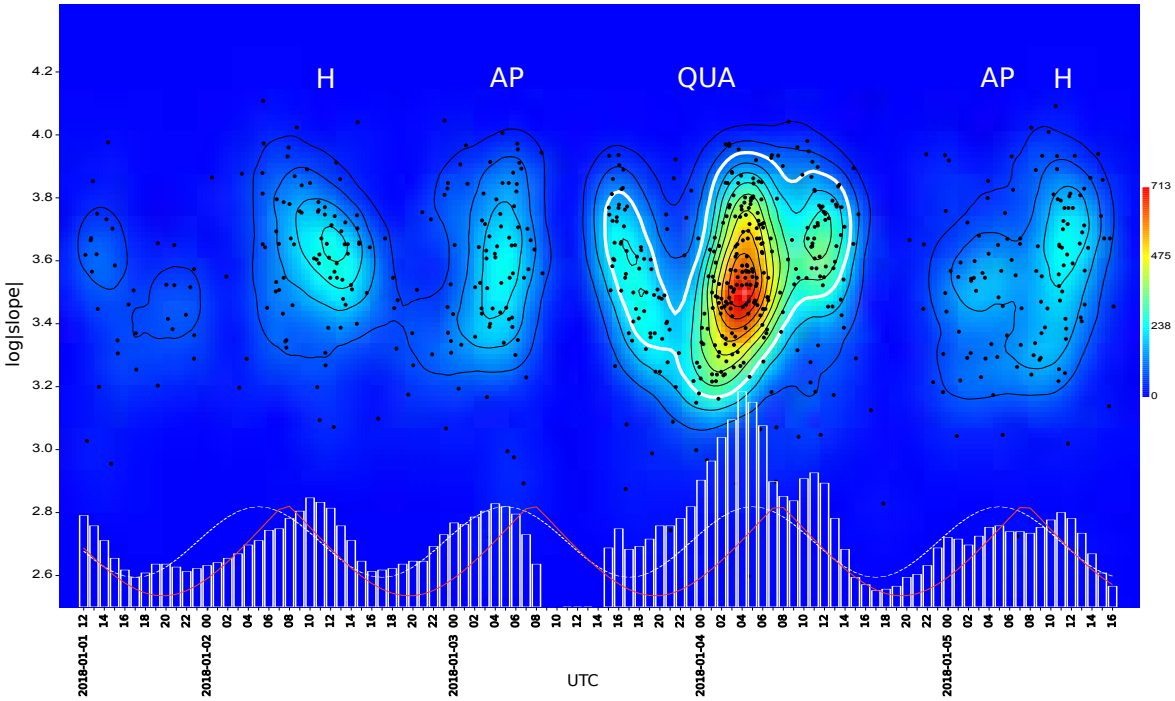

Figure 4 – Kernel density map of meteor head echoes recorded during the period 2018 January 1–5. Each dot represents the log|*slope*| of a head echo. The red line at the bottom depicts the relative course of the altitude of the radiant of the QUA. Also at the bottom the bar chart of the hourly count rates of all meteor reflections is inserted (max = 147). The white dotted line indicates the estimation of the amount of hourly sporadic meteors. The QUA can be seen as prominent hot spot. Also the helion (H) and apex (AP) source of sporadic meteors depict as weak hot spots.

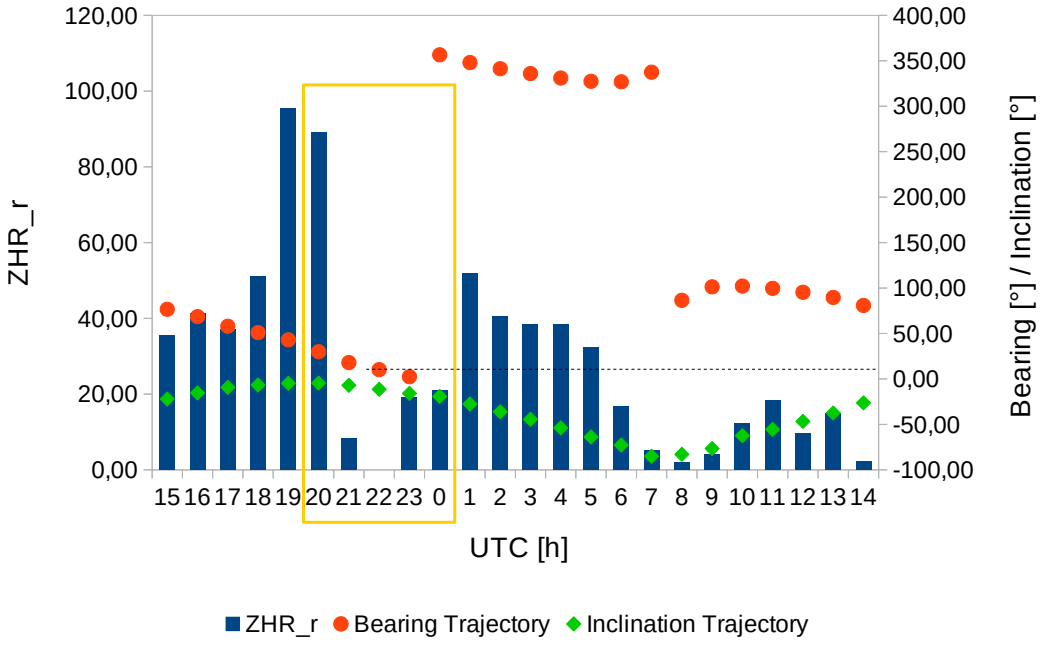

Figure 5 – Bar chart of the zenithal corrected hourly count rates of the QUA head echoes (ZHR_r) during the maximum activity in the period 2018 January 03–04. Bearing (right y-axis 0°–360°) and inclination (right y-axis −90°–0°) of the QUA-trajectories are indicated for the middle of each hour.

Acknowlegement

The author would like to thank M.T. German for inspiring him to this analysis, for intense discussions, valuable advice and helpful comments on the final draft.

References

Close S., Oppenheim M., Hunt S., and Dyrud L. (2002). "Scattering characteristics of high-resolution meteor head echoes detected at multiple frequencies". *J. Geophys. Res.*, **107:A10**, 1295.

German M. T. (2020). "A head echo Doppler model for assessment of meteoroid forward scatter characteristics". *WGN, Journal of the IMO*, **48:1**, 4–11.

Kaufmann W. (2017). "New radio meteor detecting and logging software". *WGN, Journal of the IMO*, **45:4**, 67–72.

Kaufmann W. (2018). "Visualizing meteor streams by radio forward scattering on the basis of meteor head echoes". *WGN, Journal of the IMO*, **46:1**, 39–44.

Kero J., Szasz C., Pellinen-Wannberg A., Wannberg G., Westman A., and Meisel D. D. (2008a). "Determination of meteoroid physical properties from tristatic radar observations". *Ann. Geophys.*, **26**, 2217–2228.

Kero J., Szasz C., Wannberg G., Pellinen-Wannberg A., and Westman A. (2008b). "On the meteoric head echo radar cross section angular dependence". *Geophysical Research Letters*, **35**, L07101. doi:10.1029/2008GL033402.

Rault J.-L., Birlan M., Blanpain C., Bouley S., Caminade S., Colas F., Gattacceca J., Jeanne S., Lecubin J., Malgoyre A., Marmo C., Vaubaillon J., Vernazza P., and Zanda B. (2017). "Fine-scale observations of the doppler frequency shifts affecting meteor head radio echoes". In Gyssens M. and Rault J.-L., editors, *Proceedings of the International Meteor Conference, Petnica, Serbia 21-24 September, 2017*. IMO, pages 103–106.

Rendtel J. (2014). *Meteor Shower Workbook 2014*. International Meteor Organization, Potsdam.

Rendtel J. (2017). "2018 Meteor Shower Calendar". International Meteor Organization. IMO_INFO(2-17).

Rendtel J., Ogawa H., and Sugimoto H. (2016). "Quadrantids 2016: observations of a short pre-maximum peak". *WGN, the Journal of the IMO*, **44:4**, 101–107.

Thomson W. P. (1985). "Airborne bistatic radar limitations and sample calculations". Master's thesis, Air Force Institute of Technology, Ohio.

Handling Editor: Jean-Louis Rault

Preliminary results

Results of the IMO Video Meteor Network — November 2018

Sirko Molau[1], *Stefano Crivello, Rui Goncalves, Carlos Saraiva, Enrico Stomeo, Jörg Strunk, Javor Kac*

During 2018 November, 83 cameras of the IMO Video Meteor Network recorded over 41 000 meteors during nearly 9 300 hours of observing time. The flux density profile of the Leonids is presented. It shows an activity higher than the average for the years 2011–2017. Flux density profiles are also presented for the Southern and Northern Taurids.

Received 2020 January 30

1 Introduction

The period of excellent weather, which persisted in central Europe for several months in a row, was finally over in November. The observing statistics show large gaps, and in particular in the second half of the month the observers had to accept longer interruptions. Only 37 out of the 83 active video cameras obtained observations during twenty or more nights. The total effective observing time dropped to nearly 9 300 hours – less than in the last three years. In that time, we recorded over 41 000 meteors (Table 1 and Figure 1), which is of the same order as in the preceding two years. The average of 4.4 meteors per hour is higher than last year, but lower than the long-term average (5.0).

[1]Abenstalstr. 13b, 84072 Seysdorf, Germany.
Email: sirko@molau.de

IMO bibcode WGN-481-molau-vidnov
NASA-ADS bibcode 2020JIMO...48...17M

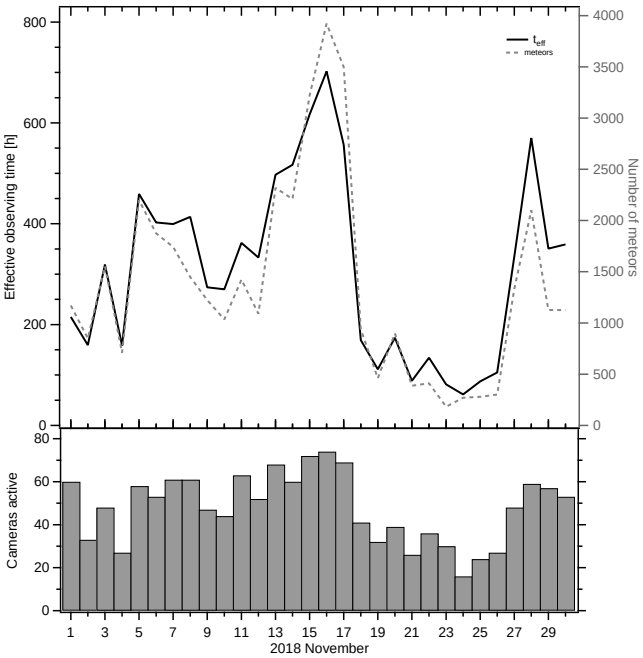

Figure 1 – Monthly summary for the effective observing time (solid black line), number of meteors (dashed gray line) and number of cameras active (bars) in 2018 November.

2 Leonids

Nearly twenty years have passed since the major outbursts of the Leonids at the turn of the millennium, which is more than half of the time to the next perihelion passage of parent comet 55P/Tempel-Tuttle. Activity of the shower has still not completely vanished – on the contrary: As Figure 2 shows, the Leonid activity of 2018 was clearly higher than in the average for the years since 2011.

During the night of November 18/19, the average flux density was 12 meteoroids per 1 000 km^2 per hour, which is twice as high as on average. We have to be cautious, because we could collect only 150 hours of effective observing time that night. However, if we look at the sporadic meteors (Figure 3) during that night we see no anomalies. In fact, the rate in 2018 was even a bit lower than in the long-term average, so the enhanced Leonid activity was real.

The IMO Meteor Shower Calendar of 2018 (Rendtel, 2017) lists differing predictions of increased Leonid activity. There are encounters predicted with a 1268 dust trail on November 18 at 23^h27^m UT and with a 1069 trail on November 19, 23^h59^m UT (Vaubaillon). On the other hand, Mikiya Sato predicted an encounter with a 1069 trail on November 19, 22^h20^m UT. Further predicted dust trail encounters fell outside the European observing window.

The small data set does not allow for a detailed analysis, particularly of when exactly rates were highest, since the radiant only reaches sufficient height to allow Leonid observations after local midnight. There is, however, a trend that the flux density was higher right after the radiant rise at midnight UT of November 18/19 when compared to the hours that followed. We can infer that the first listed dust trail caused the activity increase.

The population index of the Leonids was about $r = 1.8$ during the whole activity interval and, thus, much smaller than for the sporadic population index ($r = 2.6$).

3 Other showers

We are unable to draw conclusions about the α-Monocerotids or the November Orionids, since the gaps in the data collection are simply too large in the last third of November. However, we can have a look at

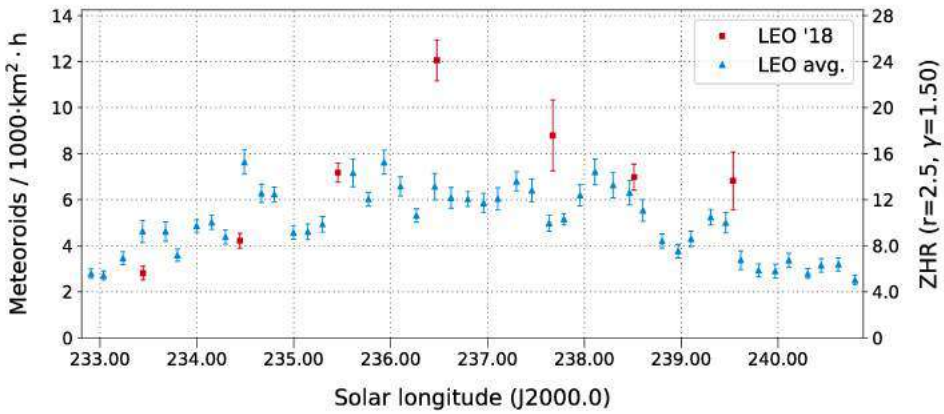

Figure 2 – Comparison of the flux density profile of the Leonids in 2018 (darker/red) and in the average of 2011–2017 (lighter/blue), derived from video data of the IMO Network.

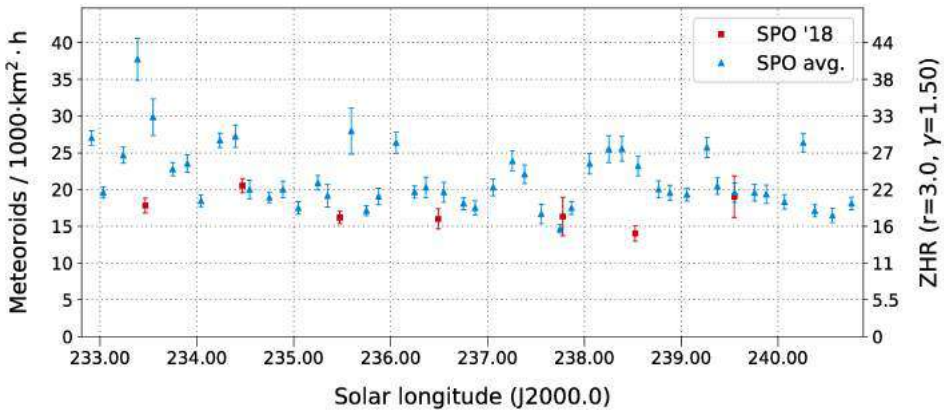

Figure 3 – Comparison of the flux density profile of the sporadic meteors at the time of the Leonids 2018 (darker/red) and in the average of 2011–2017 (lighter/blue), derived from video data of the IMO Network.

the Taurids of 2018 (Figure 4), which are active from September to November. We see the typical trend that the southern branch dominates until the end of October. Thereafter the Northern Taurids become stronger, but the scatter in the data is increasing as well. Small activity spikes in October (e.g. at 193° and 203° solar longitude) are visible in both curves, so we can assume that they are not real but rather the result from some external effect.

References

Rendtel J. (2017). "2018 Meteor Shower Calendar". International Meteor Organization. IMO_INFO(2-17).

Handling Editor: Javor Kac

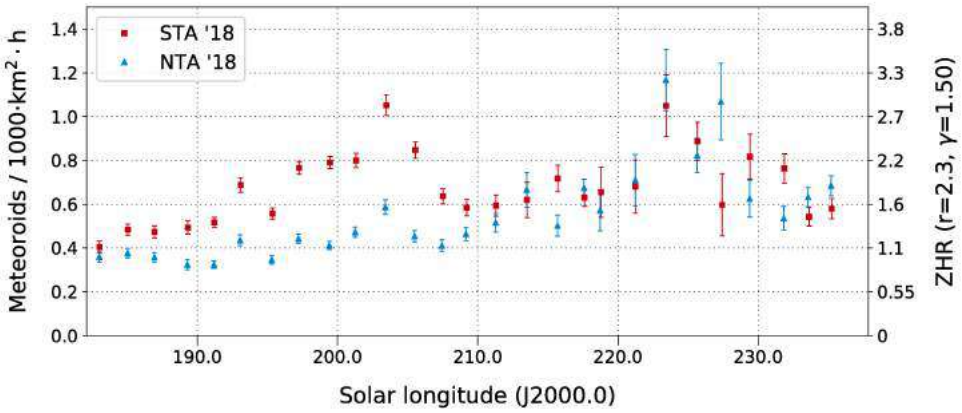

Figure 4 – Comparison of the flux density profile of the Northern (lighter/blue) and Southern (darker/red) Taurids in 2018, derived from video data of the IMO Network.

Code	Name	Location	Camera	FOV [°²]	Stellar LM [mag]	Eff.CA [km²]	Nights	Time [h]	Meteors
ARLRA	Arlt	Ludwigsfelde/DE	Ludwig2 (0.8/8)	1483	6.2	3812	21	142.3	859
BERER	Berkó	Ludányhalászi/HU	Hulud1 (0.8/3.8)	5524	4.8	3829	14	130.4	736
BIATO	Bianchi	Mt. San Lorenzo/IT	Omsl1 (1.2/4)	6422	4.0	1699	20	51.9	195
BOMMA	Bombardini	Faenza/IT	Mario (1.2/4.0)	5779	3.3	644	22	96.1	454
BREMA	Breukers	Hengelo/NL	Mbb3 (0.75/6)	2399	4.2	641	14	118.0	318
BRIBE	Klemt	Herne/DE	Hermine (0.8/6)	2369	4.2	674	24	154.7	684
		Bergisch Gladbach/DE	Klemoi (0.8/6)	2374	4.6	1123	22	142.9	579
CARMA	Carli	Monte Baldo/IT	Bmh2 (1.5/4.5)*	4243	3.0	371	20	187.5	1376
CASFL	Castellani	Monte Baldo/IT	Bmh1 (0.8/6)	2402	5.0	1633	19	165.9	545
CINFR	Cineglosso	Faenza/IT	Jenni (1.2/4)	5995	3.9	1240	23	105.3	333
CRIST	Crivello	Valbrevenna/IT	Arci (0.8/3.8)	5566	4.6	2571	22	113.8	623
			Bilbo (0.8/3.8)	5441	4.2	1764	23	129.1	829
			C3P8 (0.8/3.8)	5489	4.2	1603	20	135.0	617
			Stg38 (0.8/3.8)	5574	4.4	1905	21	72.4	559
ELTMA	Eltri	Venezia/IT	Met38 (0.8/3.8)	5607	4.3	2381	18	98.0	462
FORKE	Förster	Carlsfeld/DE	Akm3 (0.75/6)	2387	5.1	2145	21	138.4	825
GONRU	Goncalves	Foz do Arelho/PT	Farelho1 (0.75/4.5)	2260	3.0	206	8	9.9	37
		Tomar/PT	Templar1 (0.8/6)	2212	5.3	1873	22	146.1	555
			Templar2 (0.8/6)	2341	5.0	1718	22	147.7	424
			Templar3 (0.8/8)	1438	4.3	542	19	113.7	188
			Templar4 (0.8/3.8)	5180	3.0	497	20	139.4	407
			Templar5 (0.75/6)	2309	5.0	2248	23	113.3	357
GOVMI	Govedič	Središče ob Dravi/SI	Orion2 (0.8/8)	1471	5.5	2170	17	121.1	333
			Orion3 (0.95/5)	3152	4.9	2130	17	97.3	152
			Orion4 (0.95/5)	3818	4.3	1634	13	94.2	131
HERCA	Hergenrother	Tucson/US	Salsa3 (0.8/3.8)	2336	4.1	538	29	266.2	835
HINWO	Hinz	Schwarzenberg/DE	Hinwo1 (0.75/6)	2375	5.1	1889	25	195.1	863
IGAAN	Igaz	Hódmezővásárhely/HU	Huhod (0.8/3.8)	5502	3.4	764	11	68.5	192
		Budapest/HU	Hupol (1.2/4)	2414	3.6	409	17	113.3	98
JONKA	Jonas	Budapest/HU	Husor2 (0.95/3.5)	2468	3.9	716	20	166.3	306
KACJA	Kac	Kamnik/SI	Cvetka (0.8/3.8)*	5334	4.3	2028	5	30.7	210
			Rezika (0.8/6)	2269	4.4	863	5	30.5	200
			Stefka (0.8/3.8)	5458	3.6	911	4	29.2	140
		Ljubljana/SI	Sraka (0.8/6)	2348	4.8	1595	8	35.0	124
KOSDE	Koschny	La Palma/ES	Icc9 (0.85/25)*	660	6.7	2835	13	121.3	1329
			Lic2 (3.2/50)*	1933	6.5	6554	16	101.4	1161
MACMA	Maciejewski	Chełm/PL	Pav35 (0.8/3.8)	5329	4.0	1530	14	114.3	487
			Pav36 (0.8/3.8)*	5484	4.0	1501	14	111.6	438
			Pav43 (0.75/4.5)*	2251	4.7	1484	19	125.2	622
			Pav60 (0.75/4.5)	2302	5.1	1803	11	71.2	189

Table 1 – Observers contributing to 2018 November data of the IMO Video Meteor Network. Eff.CA designates the effective collection area; the overall number of nights is the number of nights with at least one camera operating, the overall observing time and number of meteors are sums over all cameras.

Table 1 – Observers contributing to 2018 November data of the IMO Video Meteor Network – continued from previous page.

Code	Name	Location	Camera	FOV [°²]	Stellar LM [mag]	Eff.CA [km²]	Nights	Time [h]	Meteors
MARRU	Marques	Lisbon/PT	Ran1 (1.4/4.5)	4395	4.0	1330	27	142.5	558
MASMI	Maslov	Novosibirsk/RU	Nowatec (0.8/3.8)	5559	3.6	827	2	14.0	64
MISST	Missiaggia	Nove/IT	Toaldo (1.2/4.5)	4329	4.6	2049	22	125.8	468
MOLSI	Molau	Seysdorf/DE	Avis2 (1.4/50)*	1204	6.9	5982	16	91.6	806
			Dimcam1 (0.8/8)	1553	6.8	10447	13	83.5	1041
			Escimo2 (0.85/25)	154	8.1	3828	13	100.2	209
		Ketzür/DE	Remo1 (0.8/8)	1467	6.5	5459	23	151.7	1199
			Remo2 (0.8/8)	1479	6.4	5037	22	155.5	1180
			Remo3 (0.8/8)	1422	6.4	4207	23	176.8	1016
			Remo4 (0.8/8)	1478	6.5	5355	25	174.3	1318
MORJO	Morvai	Fülöpszállás/HU	Huful (1.4/5)	3666	3.8	805	18	117.9	312
MOSFA	Moschini	Rovereto/IT	Rover (1.4/4.5)	3868	4.2	1240	17	99.7	280
NAGHE	Nagy	Budapest/HU	Hukon (0.8/3.8)	5475	4.0	1583	22	167.2	732
		Piszkéstető/HU	Hupis (0.8/3.8)	5622	4.0	1539	14	136.9	630
		Zamardi/HU	Huzam (0.8/6)	2359	4.7	1340	17	137.9	313
OCHPA	Ochner	Albiano/IT	Albiano (1.2/4.5)	3013	4.3	886	3	1.5	8
OTTMI	Otte	Pearl City/US	Orie1 (1.4/5.7)	2317	3.8	373	6	9.7	35
PERZS	Perkó	Becsehely/HU	Hubec (0.8/3.8)*	5557	2.9	470	14	138.8	588
ROTEC	Rothenberg	Berlin/DE	Armefa (0.8/6)	2359	4.5	907	18	132.3	276
SARAN	Saraiva	Carnaxide/PT	Ro1 (0.75/6)	2354	4.0	536	21	93.6	245
			Ro2 (0.75/6)	2365	4.1	635	15	51.6	169
			Ro3 (0.8/12)	720	5.7	1126	14	63.5	207
			Ro4 (1.0/8)	1568	4.2	546	14	55.9	65
			Sofia (0.8/12)	726	4.8	516	22	124.5	317
SCALE	Scarpa	Alberoni/IT	Leo (1.2/4.5)*	4170	4.5	2044	18	83.8	184
SCHHA	Schremmer	Niederkrüchten/DE	Doraemon (0.8/3.8)	5522	4.7	3184	24	156.3	528
SLAST	Slavec	Ljubljana/SI	Kayak1 (1.8/28)	1074	5.7	2642	9	38.9	85
			Kayak2 (0.8/12)	742	5.7	1052	9	42.9	56
STOEN	Stomeo	Scorze/IT	Min38 (0.8/3.8)	5587	4.5	2362	22	126.0	1003
			Noa38 (0.8/3.8)	5612	4.2	1889	22	139.2	930
			Sco38 (0.8/3.8)	5583	4.8	3304	21	104.7	757
STRJO	Strunk	Herford/DE	Mincam2 (0.8/6)	2355	5.6	3423	22	160.8	1224
			Mincam3 (0.8/6)	2302	4.5	1150	20	154.6	583
			Mincam4 (0.8/6)	2274	4.7	1001	21	148.8	322
			Mincam5 (0.8/6)	1481	6.0	3200	20	157.3	615
			Mincam6 (0.8/6)	2396	5.3	2748	21	154.6	648
TEPIS	Tepliczky	Agostyán/HU	Huago (0.75/4.5)	2428	4.6	1247	16	118.0	530
			Humob (0.8/6)	2388	4.6	1225	18	168.5	522
WEGWA	Wegrzyk	Nieznaszyn/PL	Pav78 (0.8/6)	2376	4.4	1264	19	137.7	427
YRJIL	Yrjölä	Kuusankoski/FI	Finexcam (0.8/6)	2315	5.5	2769	14	90.3	315
ZAKJU	Zakrajšek	Petkovec/SI	Petka (0.8/8)	1431	5.6	1956	15	65.1	337
			Tacka (0.8/12)	715	5.3	784	13	54.2	88
* active field of view smaller than video frame						Overall	30	9 282.2	41 305

Meteor Beliefs

Was Mithras "born" from a meteorite?

Jane T. Sibley [1]

One of the more enigmatic puzzles in Mithraic iconography is the question of the god's apparent birth from a large lumpy piece of stone. It is argued that it is natural to assume that this stone was thought of as a meteorite from which Mithras was not "born", but which served to transport him to Earth.

Received 2019 December 5

1 Introduction

The cult of Mithras was widespread among the military and clerical classes in the Roman Empire. One of the more enigmatic puzzles in Mithraic iconography is the question of the god's apparent birth from a large lumpy piece of stone. Was Mithras' rock simply lying about on a lower plane until it hatched, or was it some kind of vehicle or space-faring "egg" which encapsulated the full-grown god, who only emerged from it upon safely arriving at his destination? Could that stony vehicle have been a meteorite?

All notes appear at the end of the article.

2 The rock as a meteoritic vehicle

Images of the infant Mithras place him in the celestial (and purely divine) plane of existence.[1]

Here, he physically interacted with the constellations of the zodiacal ecliptic, and as yet had no dealings with the world of men. But when the god attained his full stature and maturity, it was time for him to be set on his mission. He had a critical task to perform, that of the precisely-timed Tauroctony (bull-slaying), and the revelation of this Mystery to his mortal adherents. For that purpose, Mithras had to travel or be sent in some manner from his original cosmic birthplace into a "lower" realm which interfaced with that of human mortals, the plane in which he was fated to perform the Tauroctony. The Leontocephalus (lion-headed) being, also called Aïon or the "serpent-wrapped god", the keeper of the secrets of the cosmos, was the most likely candidate for having enabled this voyage.[2]

Mithras obviously had to be transported within some kind of shell or protective vehicle; he could not make the journey on his own. He was naked except for his hat, and he also had to somehow keep his torch lit during his voyage. In ancient Persian and Zoroastrian models, gods rode/were enclosed within supernatural vehicles/emanations called *fravashi*, which were (and still are, in modern Zoroastrianism) depicted as winged disk figures with trailing fronds. In Mithras' case, this ride was apparently a one-way passage within a large rock.

Most versions of this particular rock may be crude attempts at depicting remaglypted meteorites.[3] To the ancients, remaglypts were, of course, believed to have been marks left by the fingers of a sky-god or goddess who threw the missile to Earth, such as Astarte (Tyre), Diana (Ephesius), Amun (Thebes), or Seth (Cabasa), to name a few.[4]

Meteorites have long been considered to be *lithos empsychos*, the home of a god, and many meteorites were worshiped as such.[5] We see Jupiter Lapis, "Jupiter-as-a-stone", as well as Beth-El, the ancient Semitic/Canaanite "(the god) El-in/as-a-stone/baetylos". The head of the silver statue of the goddess Ops (Cybele), honored during the time of the Roman Empire, was a black meteorite.[6] A triangular/coniform meteorite was revered as a *baetylos* in the fifth century BCE Greek city of Caria, Kaunos; a stone answering this description was recently excavated at that site.[7] In antiquity, meteorites were almost universally believed to be of obvious supernatural origin, thrown and/or inhabited by a god. The concept of a meteorite as a supernatural vehicle was common knowledge when Mithraism came into being, and it is therefore entirely probable that the *Petra Genetrix* was, in fact, a meteorite.

Aïon was originally modeled on Phanes (or Protogonos), a Parthian/Orphic deity. Phanes had been the "manifest one", the keeper of the seeds of the gods.[8] One version of Phanes (or the early Aïon?) showed the god standing atop a flaming inverted hemispherical object (a flattened meteoritic bolide?).[9] Later, Aïon had a maned lion's head with jaws slightly agape, and held keys, wards up, in his hands. In several instances, a Roman-style thunderbolt (*keraunos*) is associated with the god (applied to his chest, leaning against a leg or arm), but Aïon is never seen actually holding or throwing one. The keys, which only Aïon could turn, opened the gates of the celestial spheres, allowing passage from one side to the other.[10]

In several versions of the Tauroctony, a figure identifiable as Aïon is placed at mid-point between the row of seven fire-altars, which correspond to the seven planetary gods. A wingless Aïon may also appear next to Sol in the upper left corner of the Tauroctony.[11] In at least one instance, a naked male figure with upraised hands kneels between Sol and Aïon, facing Sol, with a rock/flame directly behind him.[12] This might logically be interpreted as Mithras as a grown young man in the celestial sphere, receiving instructions from Sol Invictus concerning the meaning and necessity of the Tauroctony just before he is sent to the lower sphere. At this point in time, Mithras and Aïon are clearly located in the celestial realms above the star-studded

[1]P.O. Box 123, Haddam, CT 06438, USA
Email: jrsibley@snet.net

IMO bibcode WGN-481-sibley-mitras
NASA-ADS bibcode 2020JIMO...48...21S

shell/barrier.[13] Since the Aïon standing next to the kneeling figure had not yet performed his task of launching Mithras down to the realm inhabited by the Bull, Cautes, and Cautopates, he could not display the attributes of the fulfilled, post-launch deity; thus, the lack of wings and thunderbolt. The second Aïon, located between the fire-altars/planetary gods, is winged and holds a staff/scepter.

Aïon is frequently seen with an ovate "pineapple" or "pine cone". This object may actually be a crude remaglypted meteorite carved by an artist who had obviously never laid eyes on one. The god may hold this item in one hand, or stand next to it.[14] Jupiter has also been seen in Mithraic friezes holding a similar "pineapple". In Jupiter's case, that item may be clearly identified as a meteorite. Later-period copies of this "pineapple", sometimes carved as a stand-alone object, are more pine cone-like than earlier examples, which suggests that these later ones were re-interpreted into a familiar form as a result of the "Xerox effect", a succession of copies of copies. Similar transformations of motifs or icons have been seen elsewhere.

Aïon occasionally stands on a smooth ovate or spheroid object. In a few cases, this sphere is encircled by one, or by two crossed belts.[15] According to Ulansey (1989), this belted version of the orb represents an emphasized zodiacal ecliptic in the starry cosmic shell within which the world of humans was found, and into which the god was tasked to launch Mithras, safely enclosed within a proven re-entry vehicle. An unbelted version (especially if it is lumpy, irregular, or flaming) might represent the meteorite before Mithras had entered it. As AÃŕon only had to throw this one missile, a keraunos next to him or applied to his chest would indicate that he did have the divine power, authority, and destiny to accomplish that particular task.

Smooth-surfaced sandstone balls have been found loose in a number of mithraea, but so far little has been said of them in the literature.[16] Could these have represented Aïon's orb, used as physical symbols which could be handled by human mortals as a part of Mithraic ritual? And the sound of a sistrum, depicted as a symbol of the Leo grade, might represent the sound of electrophonic transduction produced by the passage of a meteorite through Earth's magnetic fields. If so, might these all may have been part of the lore and secrets imparted to the Leo grade, whose symbols include a Zoroastrian-style fire spade, a sistrum, and a keraunos. Could the symbols of the Leo grade be integrated into the concept of a summons to the lion-headed Aïon to throw the Petra Genetrix as a flaming meteorite, just as Jupiter throws his supernatural thunderbolt to Earth? Note that a flaming Petra Genetrix with an emerging Mithras may be seen in the cult niche of the Dura Europos mithraeum, now housed in Yale University's Art Gallery (Figure 1).[17] This would present a significant Mystery to the holder of that grade.

Mithras rarely emerges from a smooth stone. His vehicle is usually rough-surfaced, nubbled in texture, or cross-hatched. In at least one case, however, Mithras is seen emerging from a smooth egg-like vehicle, complete with a portion of the shell atop his head like a broad hat (Figure 2).[18] When Mithras emerges from his rock, he is naked except for a Phrygian cap on his head. He holds a lit torch which had obviously having been kindled on the supernatural plane by Sol Invictus himself aloft in one hand, and in the other hand, the dagger with which he is fated to slay the bull. This dagger, which also originated in the celestial plane, had to have been made of meteoritic iron, like the dynastic Egyptian "mouth-opening" tools and ritual knives such as were found in Tutankhamon's tomb.[19] This "mouth-opening" tool released the spirit from a dead person's body; Mithras' blade released the bull's spirit from its body by opening the mouth of a wound in its shoulder. Ordinary iron could not perform that task, given the blade's actual penetration site.

Figure 1 – The Dura Europos rockbirth, Vermaseren (1956, 1960), Mon. 42.

3 Discussion and conclusion

Throughout history, meteorites have been observed, falling from the starry heavens in glorious blazing streaks, frequently accompanied by sonic and/or electrophonic noise. Recovered meteorites, many of which had odd, alien, or remaglypted surfaces, were commonly believed to have been of supernatural origin, and were worshiped as such. What would make a more significant vehicle for Mithras than a meteorite? Its rocky shell would surely protect the naked god during its fiery plunge through the cosmos. Once it had landed, the god could emerge in safety, with torch and dagger held high.

During the Tauroctony, Mithras wore a star-studded cape which billowed up behind him like the shell of the cosmos. Mithras' body was under the cape; Sol Invictus and Luna were above it. Sol Invictus had to use a raven to convey the exact timing of the blow to Mithras, as he could not do so in person, since he was on a different plane of existence. Only after the Cosmic Bull was slain could Sol Invictus meet Mithras in person and convey him back into the heavens in his radiant chariot. Since meteorites do not fly up into the heavens from the Earth, that mode of transport was out. Mithras' task was done, so he could return to his celestial home.

Figure 2 – The Housesteads rockbirth, Vermaseren (1956, 1960), Mon. 695.

Meteorites, linked to primary or powerful sky-gods such as Zeus/Jupiter, had long been objects of veneration throughout the entire Mediterranean region as emissaries or the god himself. It is only natural that a meteorite would have also encased Mithras. Aïon was the most logical being who could have provided the required magical and physical aim, launch, and power to propel that missile. Mithras was not "born" from the rock; he merely emerged from his meteorite as a butterfly emerges from its cocoon.

Notes

1. Vermaseren (1956, 1960), Mon. 985.
2. On Aïon, see Hinnels (1975); Le Glay (1981); Jackson (1985); and Beck (1988).
3. Vermaseren (1956, 1960), Mon. 353, 428, 1036, and 1113. Elsewhere, this rock may resemble a baked potato: e.g., Mon. 556, 557, 1340.
4. Newton (1897), p. 10; Norton (1994), pp. 32, 161–162.
5. In the Bible, see Genesis 28:11–19, Joshua 24:26–27, Leviticus 26:1, and Numbers 33:52. See also Oakley (1971); Chevalier and Gheerbrant (1996), pp. 83–84, 935; and Hurowitz (1997). A meteorite as *baetylos* is taken up by Oakley (1971) and by Campbell (1968), p. 198. For Zeus as a meteorite, see Blinkenberg (1911), p. 13. Meteorites appear in oter contexts as "images of the god" in the Bible, Acts 19:35; Newton (1897), pp. 8–13; and Sears (1978), pp. 1–4.
6. Newton (1897), pp. 8–12. The Black Stone of Cybele was a meteorite which had been brought to Rome accompanied by much ceremony and pomp. Once there, it was incorporated into the statue of the goddess, as her actual presence. Ops was a regional form of Cybele.
7. The Kaunos meteorite appears on the reverse of a stater pictured in Waddell (1999), p. 6, plate VIII (coin no. 75). See also Konuk (1988), pp. 222–223.
8. Guthrie (1993), p. 80.
9. Vermaseren (1956, 1960), Mon. 42. He may also stand on a rough lump (Mon. 551) or a smooth ball (Mon. 390, 543, 545, 551).
10. Vermaseren (1956, 1960), Mon. 40, 103, 144, 551; Beck (1988), pp. 63, 77. In the Barberini Tauroctony, Aïon is seen to penetrate and link the spheres of the planets and of the fixed stars: see Vermaseren (1956, 1960), Mon. 245; Beck (1988), p. 83.
11. Vermaseren (1956, 1960), Mon. 335, 1510, and an intaglio gemstone, now lost (Beck, 1988, pp. 32, 49, 66–68). In Mon. 335 and the gem, a second Aïon kneels before Sol Invictus, at the upper left. A lion mask representing Aïon has also been in the central position: see Vermaseren (1956, 1960), Mon. 390, 2198. Sol Invictus is above the sphere of the fixed stars (Beck, 1988, pp. 2–3).
12. Beck (1988), pp. 32, 46–49.
13. Beck (1988), p. 83; Ulansey (1989). See also Vermaseren (1956, 1960), Mon. 245, 310.
14. In late Roman and post-Roman England, the "pineapple" may be found (in Romanized areas) as a "stand-alone" object in funerary contexts. See Scott (1879). Similar "pineapples" also appear in Mithraic contexts: see Vermaseren (1956, 1960), Mon. 125, 659 a, b, 696. Jupiter with a similar "pine cone": Mon. 659. This corresponds with Zeus holding a meteorite: see Cook (1925), plate 35. In other scenes, a smooth ball about the relative size of a tennis ball, painted light blue in two instances, has been seen in the hand of Sol Invictus (Vermaseren, 1956, 1960, Mon. 354, 480, 483) or Mithras (Mon. 459). The sky-blue ball probably represents the shell of the stars/planets. A scene of Mithras Triumphant shows the god standing facefront, holding the dagger up with his right hand, and a globe/ball in his left (Mon. 334); this ball has no paint on it.
15. Vermaseren (1956, 1960), Mon. 40, 125, 879. The "pine cone" is also associated with Cautes (Mon. 532), a crowing rooster (Mon. 312, 532), and with a serpent (Mon. 127, 128); symbols of Spring, the good rains, and new life. The Tauroctony is commonly believed to have taken place at the vernal equinox. In a few cases, the god stands on a belted ball (Mon. 543, 665). These belts have been interpreted as the zodiacal ecliptic by Ulansey (1989). It is interesting to note that some renditions of the Tauroctony show a similar belt around the bull's torso like a girth: Vermaseren (1956, 1960), Mon. 350, 430, 556.
16. Vermaseren (1956, 1960), Mon. 1016, 1147, 1204, 1247, 1268; Campbell (1968), p. 198.
17. Vermaseren (1956, 1960), Mon. 42.
18. Vermaseren (1956, 1960), Mon. 695; Daniels (1962), especially fig. 2 on p. 110; Smith (1962).
19. Wainwright (1937), especially pp. 7–19; Bell (1969); Wilkinson (1994), p. 98, fig. 61. The Egyptian "mouth-opening" tool: Roth (1993); Wilkinson (1994).

References

Beck R. (1988). *Planetary Gods and Planetary Orders in the Mysteries of Mithra*. Brill, Leiden & New York.

Bell L. (1969). "The Egyptian hieroglyphic group: front cover symbol 'be-ni-pet' "". *Meteoritics*, **4:3**, i–ii.

Blinkenberg C. (1911). *The Thunderweapon in Religion and Folklore: A Study in Comparative Archaeology*. Cambridge University Press, Cambridge, Engl.

Campbell L. A. (1968). *Mithraic Iconography and Ideology*. Brill, Leiden.

Chevalier J. and Gheerbrant A. (1996). *The Penguin Dictionary of Symbols*. 2nd edition. Translated from the French by Buchanan-Brown J., Penguin Books, New York.

Cook A. B. (1925). *Zeus: A Study in Ancient Religion. Vol. 2. Zeus, God of the Dark Sky (Thunder and Lightning)*. Cambridge University Press, Cambridge, Engl.

Daniels C. M. (1962). "Mithras Saecularis. The Housesteads mithraeum and a fragment from Carrawburgh". *Archaeologia Aeliana, Ser. 4*, **40**, 105–115.

Guthrie W. K. C. (1993). *Orpheus and Greek Religion*. Princeton University Press, Princeton, NJ, USA.

Hinnells J. R. (1975). "Reflections on the lion-headed figure in Mithraism". In *Monumentum H. S. Nyberg, Acta Iranica, Ser. 2, Vol. 1*, Leiden. pages 333–369.

Hurowitz B. (1997). "Picturing imageless deities". *Biblical Archeological Review*, **23:3**, 46–48, 51, 68–69.

Jackson H. M. (1985). "The meaning and function of the leontocephaline in Roman Mithraism". *Numen*, **32**, 17–45.

Le Glay M. (1981). "Aion". In *Iconographicum Mythologiae Classicae*, volume 1.1, Zurich-Munich. pages 399–411.

Newton R. A. (1897). "The worship of meteorites". *American Journal of Science*, **Series 4, 3:13**, 1–14.

Norton O. R. (1994). *Rocks from Outer Space: Meteorites and Meteorite Hunters*. Mountain Press Publishing Co., Missoula, MT, USA.

Oakley K. P. (1971). "The Diopet of Ephesus". *Folklore*, **82**, 207–211.

Roth A. M. (1993). "Fingers, stars, and the 'opening of the mouth': the nature and function of the *NTRWJ*-blades". *Journal of Egyptian Archaeology*, **79**, 57–79.

Scott J. (1879). "Donations to the Museum". *Proceedings of the Society of Antiquaries of Scotland*, **13**, 267–269.

Smith D. J. (1962). "The restoration of the 'Birth of Mithras' from Housesteads". *Archaeologia Aeliana, Ser. 4*, **40**, 277–280.

Ulansey D. (1989). *The Origins of the Mithraic Mysteries*. Oxford University Press, Oxford, New York.

Vermaseren M. J. (1956, 1960). *Corpus Inscriptionum et Monumentorum Religionis Mithriacae*. Two volumes. Martinus Nijhoff, The Hague.

Waddell E. J., Ltd. (1999). *Greek, Roman, and Byzantine Coins, Catalogue no. 75*.

Wainwright G. A. (1937). "The coming of iron". *Antiquity*, **10**, 5–24.

Wilkinson R. H. (1994). *Symbol & Magic in Egyptian Art*. Thames and Hudson, New York.

Handling Editor: Marc Gyssens

The International Meteor Organization

www.imo.net

Follow us on Facebook InternationalMeteorOrganization

Follow us on Twitter @IMOMeteors

Council

President: Cis Verbeeck,
Bogaertsheide 5, 2560 Kessel, Belgium.
e-mail: cis.verbeeck@scarlet.be

Vice-President: Juraj Tóth,
Fac. Math., Phys. & Inf., Comenius Univ.,
Mlynska dolina, 84248 Bratislava, Slovakia.
e-mail: toth@fmph.uniba.sk

Secretary-General: Robert Lunsford,
14884 Quail Valley Way, El Cajon,
CA 92021-2227, USA. tel. +1 619 755 7791
e-mail: lunro.imo.usa@cox.net

Treasurer: Marc Gyssens, Heerbaan 74,
B-2530 Boechout, Belgium.
e-mail: marc.gyssens@uhasselt.be
BIC: GEBABEBB
IBAN: BE30 0014 7327 5911
Bank transfer costs are always at your expense.

Other Council members:
Javor Kac (see details under WGN)
Detlef Koschny, Zeestraat 46,
NL-2211 XH Noordwijkerhout, Netherlands.
e-mail: detlef.koschny@esa.int
Sirko Molau, Abenstalstraße 13b, D-84072
Seysdorf, Germany. e-mail: sirko@molau.de
Francisco Ocaña Gonzalez, C/ Arquitectura, 7.
28005 Madrid, Spain.
e-mail: francisco.ocana.gonzalez@gmail.com
Vincent Perlerin, 16, rue Georges Bernanos,
51100 Reims, France.
e-mail: vperlerin@gmail.com
Jean-Louis Rault, Société Astronomique de
France, 16, rue de la Vallée, 91360 Epinay sur
Orge, France. e-mail: f6agr@orange.fr
Jürgen Rendtel, Eschenweg 16, D-14476
Marquardt, Germany. e-mail: jrendtel@aip.de

Commission Directors

Visual Commission: Rainer Arlt (rarlt@aip.de)
Generic e-mail address: visual@imo.net
Electronic visual report form:
http://www.imo.net/visual/report/electronic
Video Commission: Sirko Molau (video@imo.net)
Photographic Commission: Bill Ward
(William.Ward@glasgow.ac.uk)
Generic e-mail address: photo@imo.net
Radio Commission: Jean-Louis Rault
(radio@imo.net)
Fireballs: Online fireball reports:
http://fireballs.imo.net

Webmaster

Karl Antier, e-mail: webmaster@imo.net

WGN

Editor-in-chief: Javor Kac
Na Ajdov hrib 24, SI-2310 Slovenska Bistrica,
Slovenia. e-mail: wgn@imo.net;
include METEOR in the e-mail subject line

Editorial board: Ž. Andreić, M. Argo, D.J. Asher,
F. Bettonvil, J. Correira, M. Gyssens,
C. Hergenrother, T. Heywood, J.-L. Rault,
J. Rendtel, C. Verbeeck, S. de Vet, D. Vida.

IMO Sales

Available from the Treasurer or the Electronic Shop on the IMO Website	€	$
IMO membership, including subscription to WGN Vol. 48 (2020)		
Surface mail	26	32
Air Mail (outside Europe only)	49	60
Electronic subscription only	21	25
Proceedings of the International Meteor Conference on paper		
1990, 1991, 1993, 1995, 1996, 1999, 2000, 2002, 2003, per year	9	12
2007, 2010, 2011, per year	15	20
2012, 2013, 2014, 2015 per year	25	34
Proceedings of the Meteor Orbit Determination Workshop 2006	15	20
Radio Meteor School Proceedings 2005	15	20
Handbook for Meteor Observers	15	20
Meteor Shower Workbook	12	16
Electronic media		
Meteor Beliefs Project ZIP archive	6	8

Alpha Monocerotids 2019

Composite image of the brightest 20 Alpha Monocerotids during the 2019 outburst. Image Courtesy: Peter C. Slansky.